CrossMark

The L 98-59 System: Three Transiting, Terrestrial-size Planets Orbiting a Nearby M Dwarf

Veselin B. Kostov[1,2], Joshua E. Schlieder[1], Thomas Barclay[1,3], Elisa V. Quintana[1], Knicole D. Colón[1], Jonathan Brande[1,4,59], Karen A. Collins[5], Adina D. Feinstein[6], Samuel Hadden[5], Stephen R. Kane[7], Laura Kreidberg[5], Ethan Kruse[1], Christopher Lam[1], Elisabeth Matthews[8], Benjamin T. Montet[6,60], Francisco J. Pozuelos[9,10], Keivan G. Stassun[11], Jennifer G.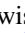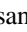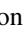 Winters[5], George Ricker[12], Roland Vanderspek[12], David Latham[5], Sara Seager[12,13,14], Joshua Winn[15], Jon M. Jenkins[16], Dennis Afanasev[17], James J. D. Armstrong[18], Giada Arney[1], Patricia Boyd[1], Geert Barentsen[19], Khalid Barkaoui[10,20], Natalie E. Batalha[21], Charles Beichman[22], Daniel Bayliss[23], Christopher Burke[8], Artem Burdanov[10], Luca Cacciapuoti[24], Andrew Carson[1], David Charbonneau[5], Jessie Christiansen[25], David Ciardi[25], Mark Clampin[1], Kevin I. Collins[26], Dennis M. Conti[27], Jeffrey Coughlin[2], Giovanni Covone[24], Ian Crossfield[12], Laetitia Delrez[28], Shawn Domagal-Goldman[1], Courtney Dressing[29], Elsa Ducrot[10], Zahra Essack[13], Mark E. Everett[30], Thomas Fauchez[1], Daniel Foreman-Mackey[31], Tianjun Gan[32], Emily Gilbert[6], Michaël Gillon[10], Erica Gonzales[21], Aaron Hamann[6], Christina Hedges[19], Hannah Hocutt[33], Kelsey Hoffman[2], Elliott P. Horch[33], Keith Horne[34], Steve Howell[16], Shane Hynes[1], Michael Ireland[35], Jonathan M. Irwin[5], Giovanni Isopi[36], Eric L. N. Jensen[37], Emmanuël Jehin[9], Lisa Kaltenegger[38], John F. Kielkopf[39], Ravi Kopparapu[1], Nikole Lewis[38], Eric Lopez[1], Jack J. Lissauer[16], Andrew W. Mann[40], Franco Mallia[36], Avi Mandell[1], Rachel A. Matson[16], Tsevi Mazeh[41], Teresa Monsue[1], Sarah E. Moran[42], Vickie Moran[1], Caroline V. Morley[43], Brett Morris[44], Philip Muirhead[45], Koji Mukai[1,3], Susan Mullally[46], Fergal Mullally[2], Catriona Murray[28], Norio Narita[47,48,49,50,51], Enric Palle[52], Daria Pidhorodetska[1], David Quinn[1], Howard Relles[5], Stephen Rinehart[1], Matthew Ritsko[1], Joseph E. Rodriguez[5], Pamela Rowden[53], Jason F. Rowe[54], Daniel Sebastian[10], Ramotholo Sefako[55], Sahar Shahaf[41], Avi Shporer[12], Naylynn Tañón Reyes[1,56], Peter Tenenbaum[2,16], Eric B. Ting[16], Joseph D. Twicken[2,16], Gerard T. van Belle[57], Laura Vega[1], Jeffrey Volosin[1], Lucianne M. Walkowicz[58], and Allison Youngblood[1]

[1] NASA Goddard Space Flight Center, Greenbelt, MD 20771, USA
[2] SETI Institute, 189 Bernardo Avenue, Suite 200, Mountain View, CA 94043, USA
[3] University of Maryland, Baltimore County, 1000 Hilltop Circle, Baltimore, MD 21250, USA
[4] University of Maryland, College Park, MD 20742, USA
[5] Harvard-Smithsonian Center for Astrophysics, 60 Garden Street, Cambridge, MA 02138, USA
[6] Department of Astronomy and Astrophysics, University of Chicago, 5640 S. Ellis Avenue, Chicago, IL 60637, USA
[7] Department of Earth and Planetary Sciences, University of California, Riverside, CA 92521, USA
[8] Kavli Institute for Astrophysics and Space Research, Massachusetts Institute of Technology, Cambridge, MA 02139, USA
[9] Space Sciences, Technologies and Astrophysics Research (STAR) Institute, Université de Liège, 19C Allée du 6 Août, B-4000 Liège, Belgium
[10] Astrobiology Research Unit, Université de Liège, 19C Allée du 6 Août, B-4000 Liège, Belgium
[11] Vanderbilt University, Nashville, TN 37240, USA
[12] Department of Physics and Kavli Institute for Astrophysics and Space Research, Massachusetts Institute of Technology, Cambridge, MA 02139, USA
[13] Department of Earth, Atmospheric and Planetary Sciences, MIT, Cambridge, MA 02139, USA
[14] Department of Aeronautics and Astronautics, MIT, Cambridge, MA 02139, USA
[15] Department of Astrophysical Sciences, Princeton University, Princeton, NJ 08544, USA
[16] NASA Ames Research Center, Moffett Field, CA 94035, USA
[17] George Washington University, 2121 I Street NW, Washington, DC 20052, USA
[18] University of Hawaii Institute for Astronomy, 34 Ohia Ku Street, Pukalani, HI 96768, USA
[19] Bay Area Environmental Research Institute, P.O. Box 25, Moffett Field, CA, USA
[20] Oukaimeden Observatory, High Energy Physics and Astrophysics Laboratory, Cadi Ayyad University, Marrakech, Morocco
[21] Department of Astronomy and Astrophysics, University of California, Santa Cruz, CA 95064, USA
[22] NASA Exoplanet Science Institute and Infrared Processing and Analysis Center, California Institute of Technology, Jet Propulsion Laboratory, Pasadena, CA 91125, USA
[23] Department of Physics, University of Warwick, Gibbet Hill Road, Coventry CV4 7AL, UK
[24] Department of Physics "Ettore Pancini," Universita di Napoli Federico II, Compl. Univ. Monte S. Angelo, I-80126 Napoli, Italy
[25] NASA Exoplanet Science Institute, California Institute of Technology, M/S 100-22, Pasadena, CA 91125, USA
[26] Department of Physics and Astronomy, Vanderbilt University, Nashville, TN 37235, USA
[27] American Association of Variable Star Observers, 49 Bay State Road, Cambridge, MA 02138, USA
[28] Cavendish Laboratory, JJ Thomson Avenue, Cambridge CB3 0HE, UK
[29] Department of Astronomy, University of California at Berkeley Berkeley, CA 94720, USA
[30] National Optical Astronomy Observatory, 950 North Cherry Avenue, Tucson, AZ 85719, USA
[31] Flatiron Institute, Center for Computational Astrophysics, New York, NY, USA
[32] Department of Physics and Tsinghua Centre for Astrophysics, Tsinghua University, Beijing, People's Republic of China
[33] Department of Physics, Southern Connecticut State University, 501 Crescent Street, New Haven, CT 06515, USA
[34] SUPA School of Physics & Astronomy, University of St Andrews, North Haugh, St Andrews, Scotland, UK
[35] Research School of Astronomy and Astrophysics, Australian National University, Canberra, ACT 2611, Australia
[36] Campo Catino Astronomical Observatory, Regione Lazio, Guarcino (FR), I-03010, Italy
[37] Department of Physics and Astronomy, Swarthmore College, Swarthmore, PA 19081, USA
[38] Carl Sagan Institute, Cornell University, Space Science Institute 312, 14850 Ithaca, NY, USA
[39] Department of Physics and Astronomy, University of Louisville, Louisville, KY 40292, USA
[40] Department of Physics and Astronomy, University of North Carolina at Chapel Hill, Chapel Hill, NC 27599, USA
[41] Tel Aviv University, P.O. Box 39040, Tel Aviv 6997801, Israel
[42] Department of Earth and Planetary Sciences, Johns Hopkins University, Baltimore, MD 21218, USA

[43] Department of Astronomy, University of Texas at Austin, Austin, TX, USA
[44] University of Washington, Department of Astronomy, Seattle, WA 98195, USA
[45] Institute for Astrophysical Research, Boston University, Boston, MA 02215, USA
[46] Space Telescope Science Institute, 3700 San Martin Drive, Baltimore, MD 21218, USA
[47] Department of Astronomy, The University of Tokyo, 7-3-1 Hongo, Bunkyo-ku, Tokyo 113-0033, Japan
[48] Astrobiology Center, 2-21-1 Osawa, Mitaka, Tokyo 181-8588, Japan
[49] JST, PRESTO, 7-3-1 Hongo, Bunkyo-ku, Tokyo 113-0033, Japan
[50] National Astronomical Observatory of Japan, 2-21-1 Osawa, Mitaka, Tokyo 181-8588, Japan
[51] Instituto de Astrofisica de Canarias, E-38205 La Laguna, Tenerife, Spain
[52] Instituto de Astrofisica de Canarias, Via Lactea sn, E-38200, La Laguna, Tenerife, Spain
[53] School of Physical Sciences, The Open University, Milton Keynes MK7 6AA, UK
[54] Bishops University, 2600 College Street, Sherbrooke, QC J1M 1Z7, Canada
[55] South African Astronomical Observatory, P.O. Box 9, Observatory 7935, South Africa
[56] San Diego Mesa College, 7250 Mesa College Drive, San Diego, CA 92111, USA
[57] Lowell Observatory, 1400 W. Mars Hill Road, Flagstaff, AZ, USA
[58] The Adler Planetarium, 1300 South Lakeshore Drive, Chicago, IL 60605, USA

Abstract

We report the *Transiting Exoplanet Survey Satellite* (*TESS*) discovery of three terrestrial-size planets transiting L 98-59 (TOI-175, TIC 307210830)—a bright M dwarf at a distance of 10.6 pc. Using the *Gaia*-measured distance and broadband photometry, we find that the host star is an M3 dwarf. Combined with the *TESS* transits from three sectors, the corresponding stellar parameters yield planet radii ranging from 0.8 $R_\oplus$ to 1.6 $R_\oplus$. All three planets have short orbital periods, ranging from 2.25 to 7.45 days with the outer pair just wide of a 2:1 period resonance. Diagnostic tests produced by the *TESS* Data Validation Report and the vetting package DAVE rule out common false-positive sources. These analyses, along with dedicated follow-up and the multiplicity of the system, lend confidence that the observed signals are caused by planets transiting L 98-59 and are not associated with other sources in the field. The L 98-59 system is interesting for a number of reasons: the host star is bright ($V =$ 11.7 mag, $K =$ 7.1 mag) and the planets are prime targets for further follow-up observations including precision radial-velocity mass measurements and future transit spectroscopy with the *James Webb Space Telescope*; the near-resonant configuration makes the system a laboratory to study planetary system dynamical evolution; and three planets of relatively similar size in the same system present an opportunity to study terrestrial planets where other variables (age, metallicity, etc.) can be held constant. L 98-59 will be observed in four more *TESS* sectors, which will provide a wealth of information on the three currently known planets and have the potential to reveal additional planets in the system.

Key words: planets and satellites: detection – stars: individual (TIC 307210830, TOI-175) – techniques: photometric

1. Introduction

The *Transiting Exoplanet Survey Satellite* (*TESS*; Ricker et al. 2015), a near all-sky transit survey that began science operations on 2018 July, is expected to find thousands of planets. This includes hundreds of small planets with radii $R < 4 R_\oplus$, around nearby, bright stars (Barclay et al. 2018; Huang et al. 2018b). During the two-year primary mission, *TESS* will monitor more than 200,000 preselected stars at 2 minute cadence and will observe additional targets spread over most of the sky ($\approx$85%) in 30 minute cadence full-frame-image (FFI) mode (Ricker et al. 2015). The spacecraft carries four identical wide-field cameras that combine to produce a nearly continuous 24° × 96° field of view (FOV). *TESS* uses this large FOV to observe 13 partially overlapping sectors per ecliptic hemisphere per year and started its survey in the southern ecliptic hemisphere. The spacecraft observes each sector for two consecutive orbits that cover an average time baseline of 27.4 days.[61] The increasing overlap of sectors toward the ecliptic poles provides continuous viewing zones (CVZs) surrounding the poles where targets receive $\approx$350 days

of coverage. The long observing duration of the *TESS* CVZs will enable the detection of smaller and longer period planets. It will also overlap with the CVZs of the *James Webb Space Telescope* (*JWST*), providing key targets for detailed characterization. In about a hundred days of observations, *TESS* has already identified more than a hundred planet candidates, provided key observations to confirm several new planets, and provided new data on known transiting systems (Dragomir et al. 2019; Gandolfi et al. 2018; Huang et al. 2018a; Nielsen et al. 2019; Shporer et al. 2019; Vanderspek et al. 2019; Wang et al. 2019; Quinn et al. 2019; Rodriguez et al. 2019).

Planets discovered around bright, nearby stars provide ideal targets for mass measurements via Doppler spectroscopy, emission, and transmission spectroscopy for atmospheric characterization, and for precise stellar characterization. Multiplanet systems provide an additional layer of information on planet formation and evolution, orbital dynamics, planetary architectures (e.g., Lissauer et al. 2011; Fabrycky et al. 2014), and in some cases mass measurements via transit timing variations (TTVs; e.g., Hadden & Lithwick 2016; Hadden et al. 2018). While NASA's *Kepler* and *K2* missions successfully discovered thousands of planets around stars in the *Kepler* field and in the vicinity of the ecliptic plane (e.g., Rowe et al. 2014; Morton et al. 2016; Livingston et al. 2018), *TESS* will perform a nearly all-sky survey focused on stars in the solar neighborhood and find the touchstone planets that will be prime

---

[59] Sellers Exoplanet Environments Collaboration.
[60] Sagan Fellow.
[61] The orbital period of *TESS* is not constant due to three-body gravitational interactions between *TESS*, the Earth, and the Moon. This leads to slightly different baselines in each sector.

targets for observations with the *Hubble Space Telescope* (*HST*), *JWST*, and future ground-based observatories (Kempton et al. 2018; Louie et al. 2018).

Here we report the *TESS* discovery of three small planets transiting the bright ($K = 7.1$ mag), nearby (10.6 pc) M3 dwarf L 98-59. This paper is organized as follows. In Section 2, we describe the *TESS* observations and data analysis, as well as our ground-based follow-up efforts. In Section 3, we discuss the properties of the system, and draw our conclusions in Section 4.

2. Observations and Data Analysis

2.1. TESS *Observations and Stellar Parameters*

TESS observed L 98-59 (TIC 307210830, TOI-175; R.A. = 08:18:07.62, decl. = −68:18:46.80 (J2000)) in Sectors 2, 5, and 8 with Camera 4. The target was added to the *TESS* Candidate Target List—a list of targets prioritized for short-cadence observations (Stassun et al. 2018)—as part of the specially curated Cool Dwarf list (Muirhead et al. 2018). The *TESS* data were processed with the Science Processing Operations Center Pipeline (SPOC; Jenkins et al. 2016) and with the MIT Quick Look Pipeline. The three candidates identified by the SPOC pipeline passed a series of data validation tests (Twicken et al. 2018; Li et al. 2019) summarized below and were made publicly available on the MIT *TESS* Data Alerts website[62] and the Mikulski Archive for Space Telescopes (MAST) *TESS* alerts page[63] as TOI-175.01, -175.02, and -175.03. These candidates had periods $P = 3.690613$ days, 7.451113 days, and 2.253014 days, and transit epochs (BTJD) = 1356.203764, 1355.2864, and 1354.906208, respectively,[64] and are referred to in the rest of the manuscript as L 98-59 c, L 98-59 d, and L 98-59 b, respectively. The SPOC simple aperture photometry (SAP) and presearch data conditioned (PDCSAP) light curves (Smith et al. 2012; Stumpe et al. 2014) of L 98-59 are shown in Figure 1.

We use the methods appropriate for M dwarfs previously used by Berta-Thompson et al. (2015), Dittmann et al. (2017), and Ment et al. (2019) to determine the stellar parameters of the host star, and adopt these parameters throughout our analysis. We estimate the mass of the star using the mass–luminosity relation in the K band from Benedict et al. (2016) to be $0.313 \pm 0.014\ M_\odot$. We then use single star mass–radius relations (Boyajian et al. 2012) to find a stellar radius of $0.312 \pm 0.014\ R_\odot$. We calculate the bolometric correction in K from Mann et al. (2015, erratum) to be 2.7 ± 0.036 mag, resulting in a bolometric luminosity for L 98-59 of $0.011 \pm 0.0004\ L_\odot$. We calculate the correction in V from Pecaut & Mamajek (2013) to be $−2.0 \pm 0.03$ mag,[65] resulting in a bolometric luminosity of $0.0115 \pm 0.0005\ L_\odot$. We adopt the mean of the two bolometric luminosities from which we calculate the luminosity of the host star to be $0.0113 \pm 0.0006\ L_\odot$ (i.e., 4.31e24 W). From the Stephan–Boltzmann law, we find an effective temperature $T_{\rm eff} = 3367 \pm 150$ K. As a comparison, we also used the relations in Mann et al. (2015) to determine an effective temperature of 3419 ± 77 K for
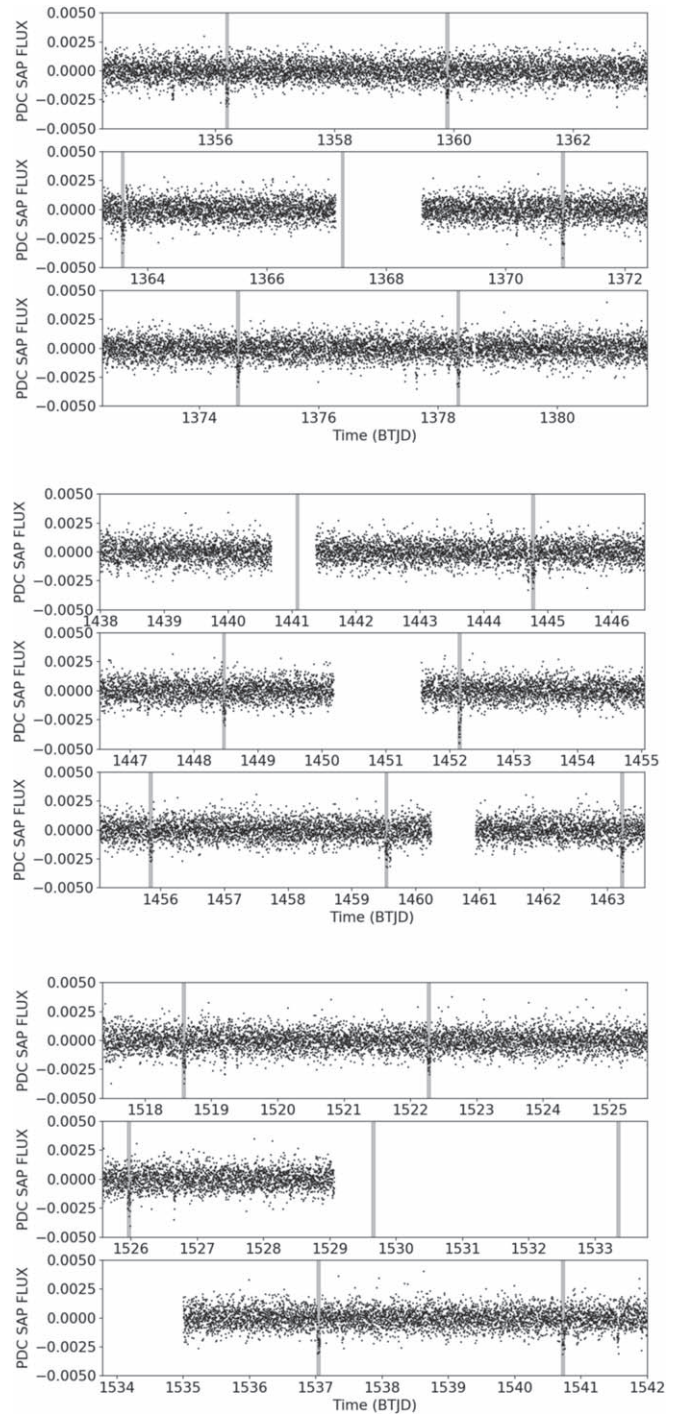

Figure 1. *TESS* PDCSAPFLUX light curves for L 98-59 as a function of time. The upper three panels represent data from Sector 2, the middle three panels from Sector 5, and the lower panels from Sector 8. For context, the transits of the planet candidate L 98-59 c are indicated with vertical gray lines. As L 98-59 c and L 98-59 d are just wide of a 2:1 period resonance, their transits can sometimes occur close to each other (e.g., around days 1445 and 1459.5), and can even create a syzygy-like configuration near day 1452.2.

L 98-59, in agreement with the $T_{\rm eff}$ derived from the Stefan–Boltzmann law.

In addition, following the procedures described in Stassun & Torres (2016) and Stassun et al. (2017) to fit a NextGen stellar atmosphere model (Hauschildt et al. 1999) to broadband photometry data from *Tycho-2*, Winters et al. (2015), *Gaia*, 2MASS, and *WISE*, we performed a full fit of the stellar spectral energy
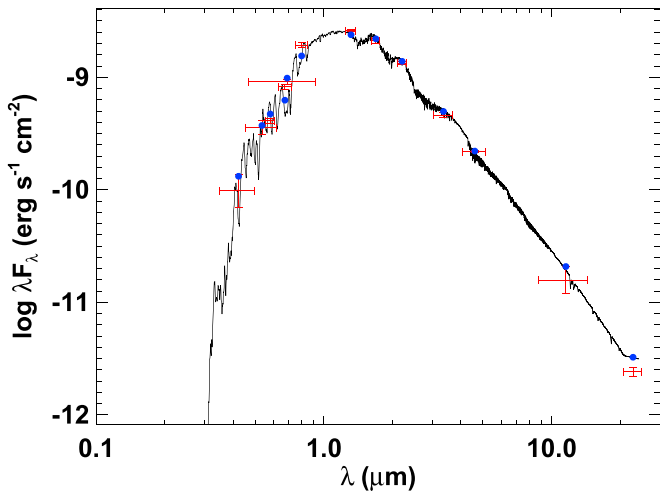
Figure 2. Spectral energy distribution (SED) fit, yielding T_{eff} and [Fe/H]. With the *Gaia* DR2 parallax, the F_{bol} from integrating SED then gives the stellar radius. The solid curve is the best-fitting NextGen atmosphere, the red symbols are the observed broadband fluxes, and the blue points are the integrated model fluxes.

distribution (SED) to estimate the stellar T_{eff} and [Fe/H] which, together with the *Gaia* DR2 parallax, provides an estimate of the stellar radius. The free parameters of the fit were T_{eff} and stellar metallicity [Fe/H], and we set the extinction $A_V \equiv 0$, due to the very close distance of the system. The resulting best fit is shown in Figure 2, with a reduced χ^2 of 3.8 for eight degrees of freedom. The best-fit parameters are $T_{eff} = 3350 \pm 100$ K and [Fe/H] = -0.5 ± 0.5. Integrating the SED gives the bolometric flux at Earth as $F_{bol} = 2.99 \pm 0.18 \times 10^{-9}$ erg s^{-1} cm^{-2}. Finally, adopting the *Gaia* DR2 parallax and the correction of 80 μas from Stassun & Torres (2018), we calculate a stellar radius of $0.305 \pm 0.018\ R_\odot$ using the Stefan–Boltzmann law. These are consistent with the adopted parameters discussed above.

We also estimated a prior on the stellar density (ρ_*) by estimating the stellar mass. Here we used the empirical relations of Mann et al. (2015), which provide $M_{star} \approx 0.32 M_\odot$ from the absolute K_S magnitude (M_{K_S}) determined from the observed 2MASS K_S magnitude and the *Gaia* DR2 parallax (corrected for the offset from Stassun & Torres 2018). The quoted uncertainty in the Mann et al. empirical relation is ∼3%; here we conservatively adopt an uncertainty of 10%. Together with the radius determined above from the SED and parallax, we obtain $\rho_* = 15.9 \pm 3.3$ g cm^{-3} (this value is used as a prior in the transit model). We also determined the stellar temperature and radius using empirical relations calibrated using low-mass stars with interferometrically measured radii and precise distances (see Feinstein et al. 2019 and references therein). These alternative stellar parameter estimates were consistent with those determined from the empirical M-dwarf relations and from the SED fitting. An additional set of stellar parameters for L 98-59 were previously derived from a medium-resolution optical spectrum in the CONCH-SHELL survey (Gaidos et al. 2014). This work also provides parameters consistent with our estimates. We compile the stellar parameters used in subsequent analyses and other identifying information for L 98-59 in Table 1. While it is difficult to pin down the ages of old M dwarfs, due to their long main-sequence lifetime, the lack of a rapid rotation signal in the *TESS* SAP light curve and the low activity of L 98-59 (see Section 2.4) indicate that it is likely an old M dwarf with age >1 Gyr. The stellar parameters of L 98-59 are consistent with a spectral type of M3 $\pm$ 1.

Table 1
Stellar Parameters

Parameter	Value	Notes
Identifying Information		
Name	L 98-59	…
TIC ID	307210830	…
TOI ID	175	…
α R.A. (hh:mm:ss)	08:18:07.62	*Gaia* DR2
δ Decl. (dd:mm:ss)	$-68:18:46.80$	*Gaia* DR2
μ_α (mas yr^{-1})	94.767 ± 0.054	*Gaia* DR2
μ_δ (mas yr^{-1})	-340.470 ± 0.052	*Gaia* DR2
Distance (pc)	10.623 ± 0.003	*Gaia* DR2
Photometric Properties		
B (mag)	13.289 ± 0.027	APASS DR9
V (mag)	11.685 ± 0.017	APASS DR9
G (mag)	10.598 ± 0.001	*Gaia* DR2
g' (mag)	12.453 ± 0.019	APASS DR9
r' (mag)	11.065 ± 0.044	APASS DR9
T (mag)	9.393	TIC
J (mag)	7.933 ± 0.027	2MASS
H (mag)	7.359 ± 0.049	2MASS
K_s (mag)	7.101 ± 0.018	2MASS
$W1$ (mag)	6.935 ± 0.062	ALLWISE
$W2$ (mag)	6.767 ± 0.021	ALLWISE
$W3$ (mag)	6.703 ± 0.016	ALLWISE
$W4$ (mag)	6.578 ± 0.047	ALLWISE
Stellar Properties		
Spectral Type	M3V $\pm$ 1	This Work
T_{eff} (K)	3367 ± 150	This Work
[Fe/H]	-0.5 ± 0.5	This Work
M_{star} ($M_\odot$)	0.313 ± 0.014	This Work
R_{star} ($R_\odot$)	0.312 ± 0.014	This Work
L_{star} ($L_\odot$)	0.0113 ± 0.0006	This Work

Note. *Gaia* DR2—Gaia Collaboration et al. (2018), UCAC5—Zacharias et al. (2017), APASS DR9—Henden et al. (2016), 2MASS—Skrutskie et al. (2006), ALLWISE—Cutri et al. (2013).

2.2. Light-curve Analyses

We opted to create our own apertures from target pixel file data from Sectors 2, 5, and 8 to analyze the photometric time series from *TESS*, instead of using the pipeline apertures used to first identify the transiting planet candidates. Our primary motivation for performing our own photometry is that we can avoid any attenuation to the transit signals by explicitly masking them during the systematic correction step. We first used the lightkurve package (Lightkurve Collaboration et al. 2018)[66] to extract light curves from each of the three sectors using the threshold method, which selects pixels that (a) are a fixed number of standard deviations above the background, and (b) create a contiguous region with the central pixel in the mask. We used a threshold value of 3σ; the corresponding mask shape is shown in Figure 3. Thus produced, the resulting light curve still contains low-level instrumental systematic signals. To identify and subtract instrumental signals, we used a second-order pixel-level de-correlation (PLD), which is a technique based on *Spitzer* and *K2* analysis methods (Deming et al. 2015; Luger et al. 2016). During the PLD step, we masked out transits to avoid attenuating the signals. Finally, we normalized the light curve by dividing by the median and
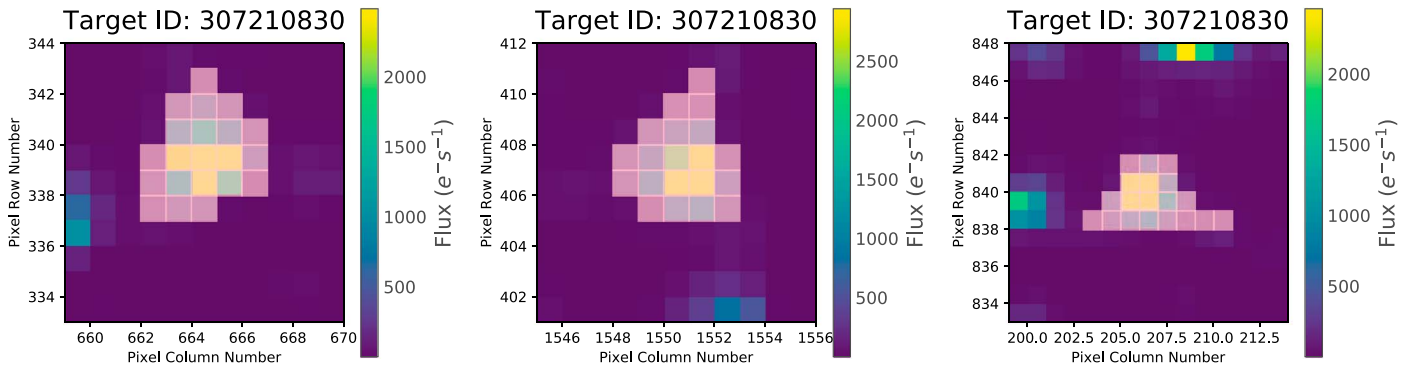
---

[66] https://github.com/KeplerGO/lightkurve

Figure 3. The pixel mask (pink squares) we used to create a light curve of L 98-59. The mask was created using the threshold method in the lightkurve extract aperture photometry tool. The three images shown are from *TESS* Sectors 2, 5, and 8.

subtracting one to center the flux about zero. We did the PLD detrending separately for each sector.

We used the exoplanet toolkit for probabilistic modeling of the exoplanet transits (Foreman-Mackey 2018). The model we built consisted of four elements: three planet transit components with Keplerian orbits and limb-darkened transits, and a Gaussian process (GP) component that models residual stellar variability. The planet models were computed with exoplanet using STARRY (Luger et al. 2019), while the GP was computed using celerite (Foreman-Mackey et al. 2017; Foreman-Mackey 2018). The GP component is described as a stochastically driven, damped harmonic oscillator with parameters of log (S_0) and log(ω_0), where the power spectrum of the GP is

$$S(\omega) = \sqrt{\frac{2}{\pi}} \frac{S_0 \, \omega_0^4}{(\omega^2 - \omega_0^2)^2 + \omega^2 \, \omega_0^2/Q^2}, \qquad (1)$$

and a white noise term, with a model parameter of the log variance. We fixed Q to $1/\sqrt{2}$ and put wide Gaussian priors on log(S_0) and log(ω_0) with the means of the log of the variance and one log of one-tenth of a cycle, respectively, and a standard deviation on the priors of 10. For each sector, we used separate GP parameters. This form of GP was chosen because of its flexible nature and it smoothly varies (it is once mean square differentiable), enabling us to use it to model a wide range of low-frequency astrophysical and instrumental signals. The white noise term carried the same prior as log(S_0). Each sector of data had a separate parameter for the mean flux level.

The planet model was parameterized in terms of consistent limb darkening, log of the stellar density, and stellar radius for the three planets. Each individual planet was parameterized in terms of the log of the orbital period, time of first transit, the log of the planet-to-star radius ratio, impact parameter, orbital eccentricity, and periastron angle at time of transit. The stellar radius had a Gaussian prior with mean 0.312 and 0.014 standard deviation, with solar units, and is in addition required to be positive. The log of the mean stellar density, in cgs units, had a Gaussian prior with a mean of log 15 and standard deviation of 0.2 dex (as per Section 2.1). The limb darkening followed the Kipping (2013a) parameterization.

The log of the orbital periods, the time of first transits, and the log of the planet-to-star radius ratio of the three planets had Gaussian priors with means at the values found in the *TESS* alert data and standard deviations of 0.1, 0.1, and 1,

respectively. The impact parameter had a uniform prior between zero and one plus the planet-to-star radius ratio. Eccentricity had a beta prior with $\alpha = 0.867$ and $\beta = 3.03$ (as suggested by Kipping 2013b), and was bound between zero and one. The periastron angle at transit was sampled in vector space to avoid the sampler seeing a discontinuity at values of π.

We sampled the posterior distribution of the model parameters using the No U-turn Sampler (NUTS; Hoffman & Gelman 2014), which is a form of Hamiltonian Monte Carlo, as implemented in PyMC3 (Salvatier et al. 2016). We ran four simultaneous chains, with 5000 tuning steps, and 3000 draws in the final sample. The effective number of independent samples of every parameter was above 1000, and most parameters were above 5000. The Gelman–Rubin diagnostic statistic was within 0.005 of 1.000 for each parameter in the model. The impact parameter for the outer planet is relatively high, which caused this parameter along with the orbital eccentricity to be the most time consuming to sample independently.

Figure 4 shows the GP model of the low-level variability in the upper panels and the best-fitting transit model in the central panels. The phase-folded transits of the three candidates, along with the best-fitting transit models, are shown in Figure 5, and the model parameters are provided in Table 2. The transit modeling reveals that the candidate planets have small radii ranging from 0.8 to 1.6 $R_\oplus$. A chain of small terrestrial-size planets is common among M dwarfs (Muirhead et al. 2015), and L 98-59 is reminiscent of other systems such as TRAPPIST-1, Kepler-186, and Kepler-296 (Quintana et al. 2014; Barclay et al. 2015; Gillon et al. 2017). The stellar density obtained from the transit model is fully consistent with that determined from the stellar parameters in Section 2.1 ($15.8^{+2.6}_{-2.7}$ g cm^{-3} for the former versus 15.9 ± 3.3 g cm^{-3} for the latter).

We repeated this analysis using the systematics-corrected light curves from the *TESS* pipeline (PDCSAP; Stumpe et al. 2014; Jenkins et al. 2016) rather than using the respective target pixel files. We found consistent results, aside from different GP parameters, owing to the different systematics corrections applied. The transit depths were lower in the PDCSAP data at the $<1\sigma$ level, which we attribute to masking out transits in the systematics-correction technique we applied. We did not include any flux contamination from nearby stars in our models because there are no bright nearby stars to contaminate our pixel mask—the TIC estimates that the contamination fraction for L 98-59 is 0.002. Even if the TIC contamination is
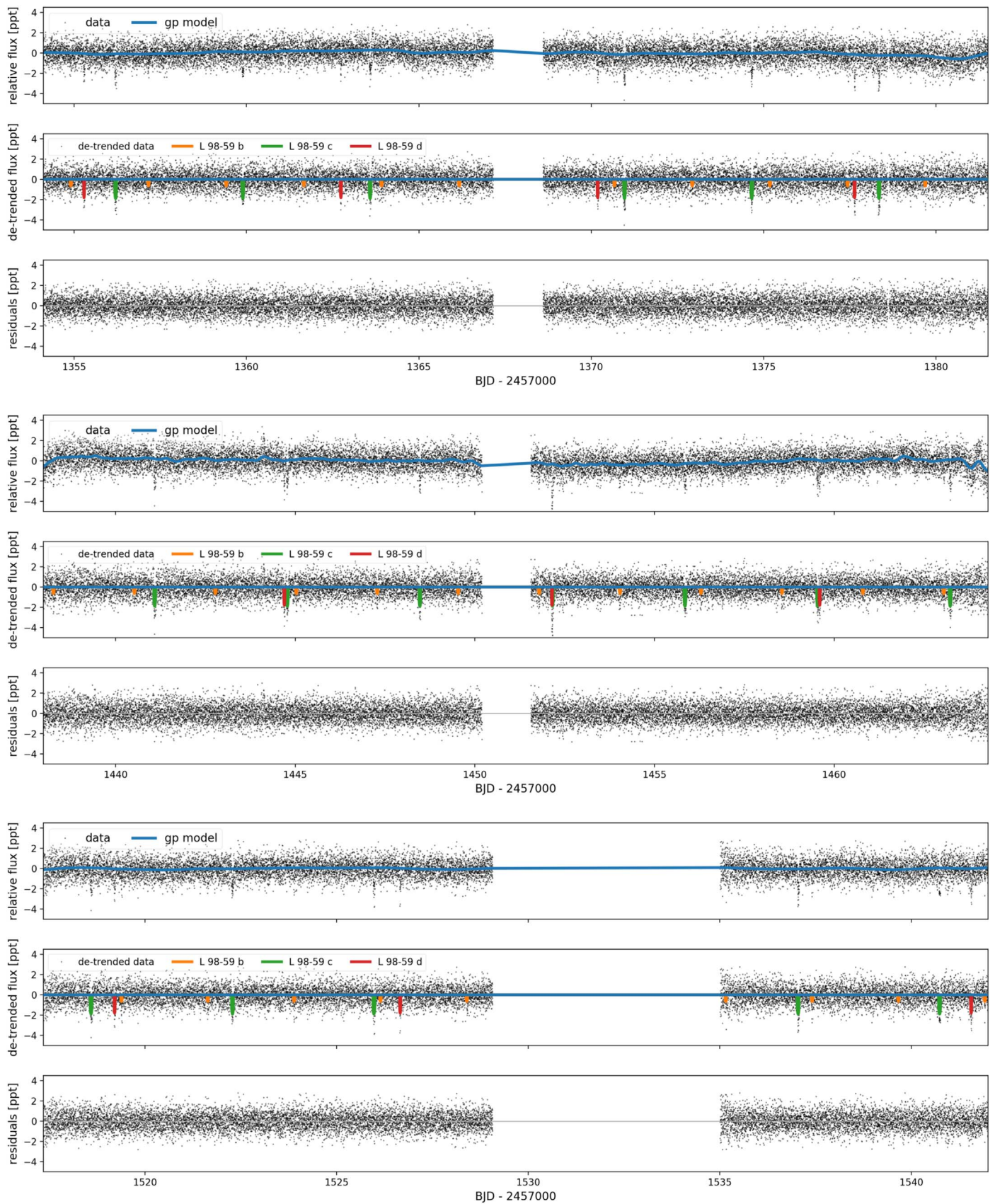
Figure 4. *TESS* data of L 98-59 from Sectors 2, 5, and 8. The top panels show the data after they have been extracted from the *TESS* target pixel file and detrended using the PLD algorithm. The green line shows the best-fitting GP mean model. In the central panels, we show the data with a GP mean model subtracted (this subtraction is only performed for display purposes in this figure). The best-fitting models for the three planets are also shown. The lower panels have the GP and planet models removed.
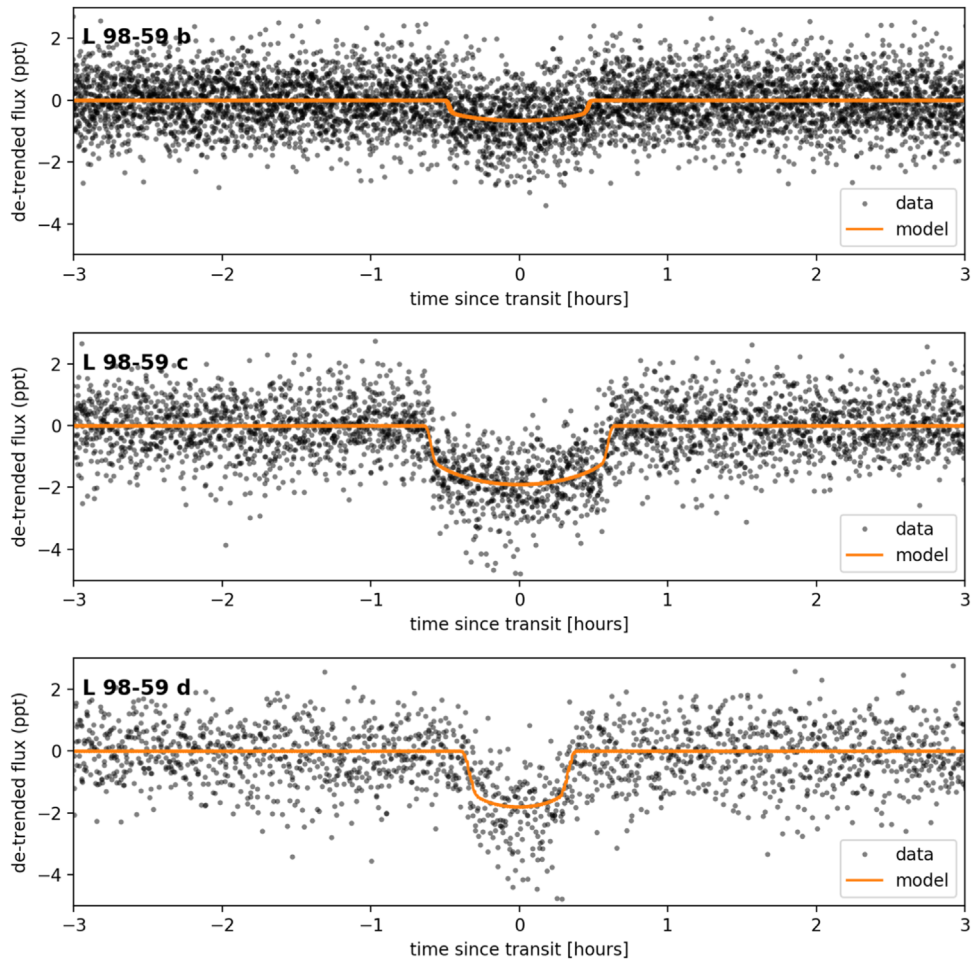
Figure 5. Phase-folded, three-sector light curves for planet L 98-59 b (upper panel), L 98-59 c (middle panel), and L 98-59 d (lower panel), along with the respective best-fitting models (orange). The corresponding transit parameters are listed in Table 2.

dramatically underestimated, it is highly likely that the stellar radius uncertainty will be the dominant term in the planet radius uncertainty; therefore, we feel comfortable ignoring it.

There are significant impact parameter differences between the inner two planets and the outer planet. The outer planet transits close to the limb of the star, although it is not grazing. This manifests in the light curve as a shorter transit duration for the outer planet than the two inner planets and indicates a modest mutual inclination of at least one degree between the inner two and outer planets. All three planets are subject to significantly more flux than Earth receives from the Sun, and are therefore unlikely to be good astrobiology targets. However, with an insolation flux of 4.5 ± 0.8, the outer planet is a candidate Venus-zone planet (Kane et al. 2014).

2.3. Potential False-positive Scenarios

The *TESS* Data Validation Report performs a series of tests designed to rule out various false-positive scenarios. The results from these tests are as follows:

(i) L 98-59 c and L 98-59 d pass the difference image centroiding test, which employs PSF-based centroiding on the difference images (expected to be more precise and accurate than a brightness-weighted moment on the difference images). While L 98-59 b does not quite pass

the difference image centroiding test, its transits are much shallower compared to the other two candidates. Thus, it is likely that the centroiding errors are underestimated to some degree, due to the variable pointing performance at timescales less than the 2 minute observation cadence. We expect the analysis of this candidate to improve with new data.

(ii) All three candidates pass the odd–even difference tests.

(iii) Secondary eclipses are ruled out at the 3.6σ, 2.6σ, and 1.8σ levels.

(iv) A bootstrap analysis of the out-of-transit data is used to quantify the probability of false alarms, due to stellar variability and residual instrumental systematics. In the case of L 98-59, the light curve is well behaved and the analysis excludes the possibility of a false alarm at the 2.45E–25, 6.6E–62, and 2.2E–25 levels (as extrapolations of the upper tail of the bootstrap distribution to the observed maximum Multiple Event Statistics (MES) that triggered the detections of these candidates in the pipeline; Jenkins et al. 2017).

(v) All three candidates pass a ghost diagnostic test, designed to flag instances of scattered light, other instrumental artifacts, or background eclipsing binaries.

For completeness, we also applied the vetting pipeline DAVE (Kostov et al. 2019) to the *TESS* light curve of L 98-59.

Table 2
Planet Parameters

Parameter	-1σ	Median	$+1\sigma$
Model Parameters			
Star			
ln ρ (g cm^{-3})	2.57	2.76	2.91
Limb darkening q_1	0.41	0.65	0.83
Limb darkening q_2	−0.34	−0.11	0.28
L 98-59 b			
T_0 (BJD-2457000)	1366.1694	1366.1701	1366.1707
ln period (days)	0.812318	0.812326	0.812334
Impact parameter	0.13	0.36	0.55
ln R_p/R_*	−3.79	−3.75	−3.72
Eccentricity	0.03	0.10	0.27
ω (rad)	−2.2	0.3	2.4
L 98-59 c			
T_0 (BJD-2457000)	1367.2752	1367.2755	1367.2759
ln period (days)	1.305791	1.305795	1.305798
Impact parameter	0.09	0.29	0.49
ln R_p/R_*	−3.25	−3.23	−3.20
Eccentricity	0.02	0.09	0.25
ω (rad)	−2.5	−0.4	2.2
L 98-59 d			
T_0 (BJD-2457000)	1362.7367	1362.7375	1362.7382
ln period (days)	2.008323	2.008329	2.008334
Impact parameter	0.75	0.89	0.93
ln R_p/R_*	−3.16	−3.07	−3.01
Eccentricity	0.04	0.20	0.52
ω (rad)	−1.9	0.7	2.3
Derived Parameters			
L 98-59 b			
Period (days)	2.25312	2.25314	2.25316
R_p/R_*	0.0226	0.0234	0.0243
Radius ($R_\oplus$)	0.75	0.80	0.85
Insolation	19.5	23.9	29.2
a/R_*	15.2	16.2	17.0
a (au)	0.0216	0.0233	0.0250
Inclination (deg)	88.0	88.7	89.5
Duration (hr)	0.89	1.02	1.19
L 98-59 c			
Period (days)	3.690607	3.690621	3.690634
R_p/R_*	0.0388	0.0396	0.0407
Radius ($R_\oplus$)	1.28	1.35	1.43
Insolation	10.1	12.4	15.2
a/R_*	21.1	22.5	23.6
a (au)	0.0300	0.0324	0.0347
Inclination (deg)	88.8	89.3	89.7
Duration (hr)	1.07	1.24	1.36
L 98-59 d			
Period (days)	7.45081	7.45086	7.45090
R_p/R_*	0.0426	0.0462	0.0492
Radius ($R_\oplus$)	1.43	1.57	1.71
Insolation	3.96	4.85	5.93
a/R_*	36.2	37.4	38.5
a (au)	0.048	0.052	0.056
Inclination (deg)	88.0	88.5	88.7
Duration (hr)	0.74	0.91	1.68

Briefly, DAVE evaluates whether detected transit-like events produced by the candidate are real or false positives by analyzing the data for (a) odd–even differences between consecutive transits, (b) secondary eclipses, (c) stellar variability mimicking a transit, and (d) photocenter shifts during transit.

To perform the (a)–(c) analysis, we used the Modelshift module of DAVE—an automated package designed to emphasize features in the light curve that resemble the shape, depth, and duration of the planetary transit but located at different orbital phase. To identify secondary eclipses and odd–even transit differences, or flares and heartbeat stars (see e.g., Welsh et al. 2011), Modelshift first convolves the light curve with the transit model of the planet candidate. The module then computes the significance of the primary transits; odd–even differences; and secondary, tertiary, and positive features assuming white noise in the light curve; and compares the ratio between each of these and the systematic red noise $F_{\rm red}$ to the false alarm thresholds $FA_1 = \sqrt{2}\,{\rm erfcinv}(T_{\rm dur}/(P \times N))$ (assuming 20,000 objects evaluated) and $FA_2 = \sqrt{2}\,{\rm erfcinv}(T_{\rm dur}/P)$ (for two events), where $T_{\rm dur}$, P, and N are the duration, period, and number of events (see Coughlin et al. 2014 for details). For example, a secondary feature is considered significant if $Sec/F_{\rm red} > FA_1$. The Modelshift results are shown in Figures 6–8, where the panels show the phase-folded light curve (first row), the phase-folded light curve convolved with the best-fit transit model (second row), as well as the the best-fit to all primary transits, all odd and all even transits, and the most prominent secondary, tertiary, and positive features in the light curve (lower two rows). The tables above the figures list the individual features evaluated by the module: the significance of the primary ("Pri"), secondary ("Sec"), tertiary ("Ter"), and positive ("Pos") events assuming white noise, along with their corresponding differences ("Pri-Ter," "Pri-Pos," "Sec-Ter," "Sec-Pos"), the significance of the odd–even metric ("Odd-Evn"), the ratio of the individual depths' median and mean values ("DMM"), the shape metric ("Shape"), the False Alarm thresholds ("FA_1," "FA_2"), and the ratio of the red noise to the white noise in the phased light curve at the transit timescale ("Fred"). Our analysis shows that there are no secondary eclipses or odd–even differences for any of the L 98-59 planet candidates. We note that the significant secondary and tertiary eclipses identified by DAVE for L 98-59 d (Figure 7) are due to the transits of L 98-59 c and thus not a source of concern.

To perform the (d) analysis for each candidate, we used the photocenter module of DAVE, following the prescription of Bryson et al. (2013). Specifically, for each candidate we (1) create the mean in-transit and out-of-transit images for each transit (ignoring cadences with nonzero quality flags), where the latter are based on the same number of exposure cadences as the former, split evenly before and after the transit; (2) calculate the overall mean in-transit and out-of-transit images by averaging over all transits; (3) subtract the overall mean out-of-transit image from the overall in-transit image to produce the overall mean difference image; and (4) measure the center of light for each difference and out-of-transit image by calculating the corresponding x and y moments of the image. The measured photocenters for the three planet candidates are shown in Figures 9–11 and listed in Table 3. We detect no significant photocenter shifts between the respective difference images and out-of-transit images for any of the planet candidates (see Table 3), which confirms that the target star is the source of the transits. We note that some of the individual difference images for L 98-59 b deviate from the expected Gaussian profile, and thus, so does the mean difference image.

Overall, our DAVE results rule out false-positive features for all three planet candidates of L 98-59, are consistent with the analysis of the Data Validation Report, and indicate that the detected events are genuine transits associated with the star
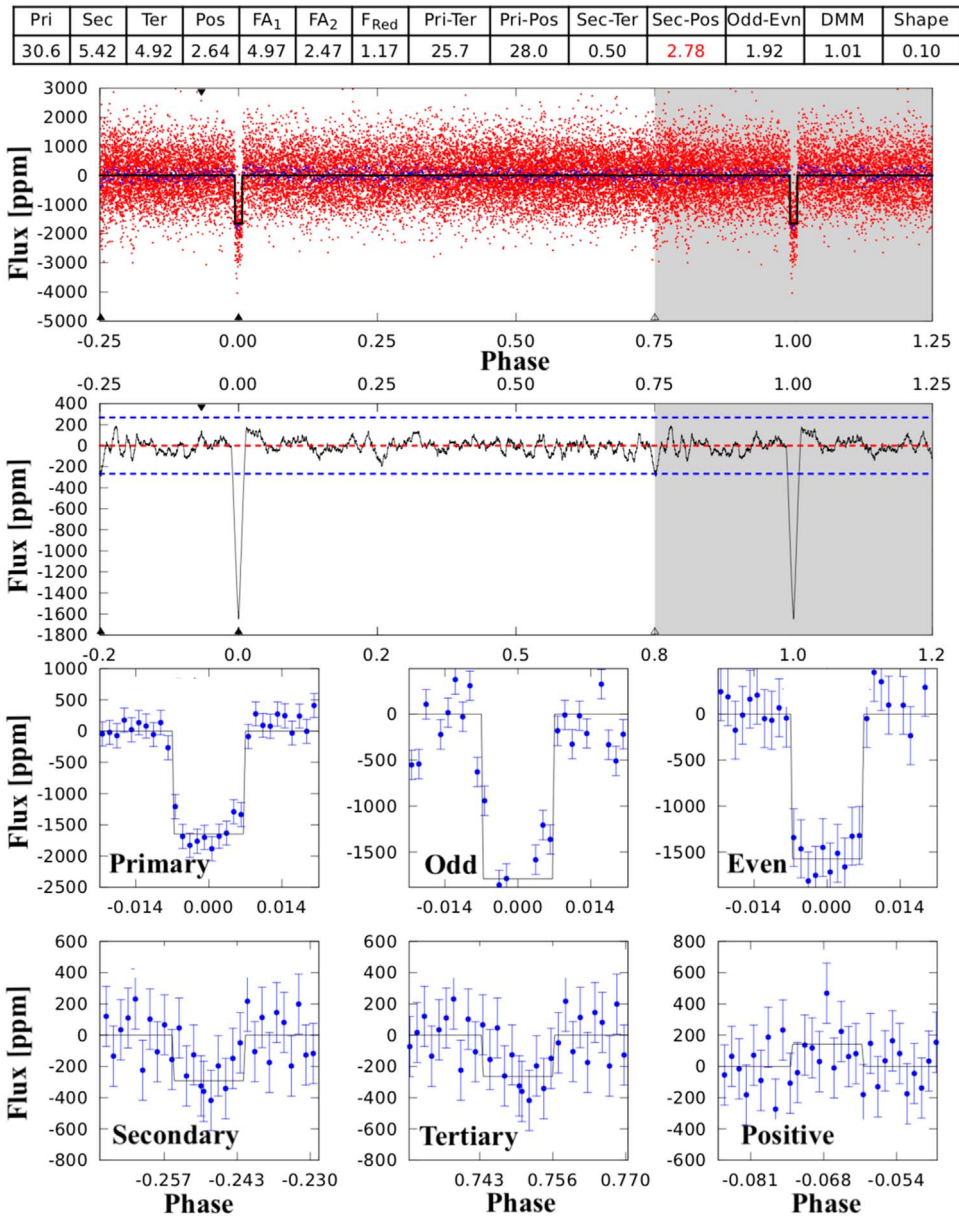
Pri	Sec	Ter	Pos	FA$_1$	FA$_2$	F$_{Red}$	Pri-Ter	Pri-Pos	Sec-Ter	Sec-Pos	Odd-Evn	DMM	Shape
30.6	5.42	4.92	2.64	4.97	2.47	1.17	25.7	28.0	0.50	2.78	1.92	1.01	0.10

Figure 6. DAVE Modelshift analysis of L 98-59 c. The upper two rows represent the phase-folded light curve with the best-fit transit model (first row), and the phase-folded light curve convolved with the best-fit transit model (second row). The six panels in the lower two rows show all transits (label "Primary"), all odd transits ("Odd"), all even transits ("Even"), and the most significant secondary ("Secondary"), tertiary ("Tertiary"), and ("Positive") features in the light curve. The table above the figure lists the significance of each feature (see text for details). There are no significant odd–even differences, secondary eclipses, or photocenter shifts, indicating that the transit events are consistent with genuine planet candidates.

in question. We also note that while the automated vetting of Osborn et al. (2019) flagged L 98-59 with "a high likelihood of being astrophysical false positives" (their Table 3), their subsequent manual vetting lists the system as a planet candidate.

Additionally, to investigate whether one or more of the transits associated with L 98-59 may result from nearby sources (e.g., a background eclipsing binary), we used lightkurve to extract light curves for nearby field stars. Our analysis revealed that a nearby field star $\sim 80''$ NW of L 98-59 (2MASS 08175808-6817459, TIC 307210817, Tmag = 13.45, i.e., ≈ 4 mag fainter than L 98-59) is in fact an eclipsing binary (EB), manifesting both primary and secondary eclipses at a period of ≈ 10.43 days, with $T_0 = 4.4309$ (BJD-2,455,000) (see Figure 12). This field star could be associated with one of two sources in the *Gaia* catalog: source 1 with R.A. = 124.492171 49500, decl. = −68.29612321000, ID = 527105568554179 7120, and parallax = 0.1888 mas; and source 2 with R.A. = 124.49126472300, decl. = −68.29602748080, ID = 5271055689840223744, and parallax = 0.9977 mas. Given the corresponding approximate distances of 1 and 5 kpc, neither of these targets can be physically associated with L 98-59 as they lie deep in the background. Regardless of which of these sources hosts the detected EB, the faintness of the host compared to L 98-59, the measured EB orbital parameters, and the dilution-corrected eclipse depths are inconsistent with the properties of the candidate planets and effectively rule it out as the potential source of any of these signals.
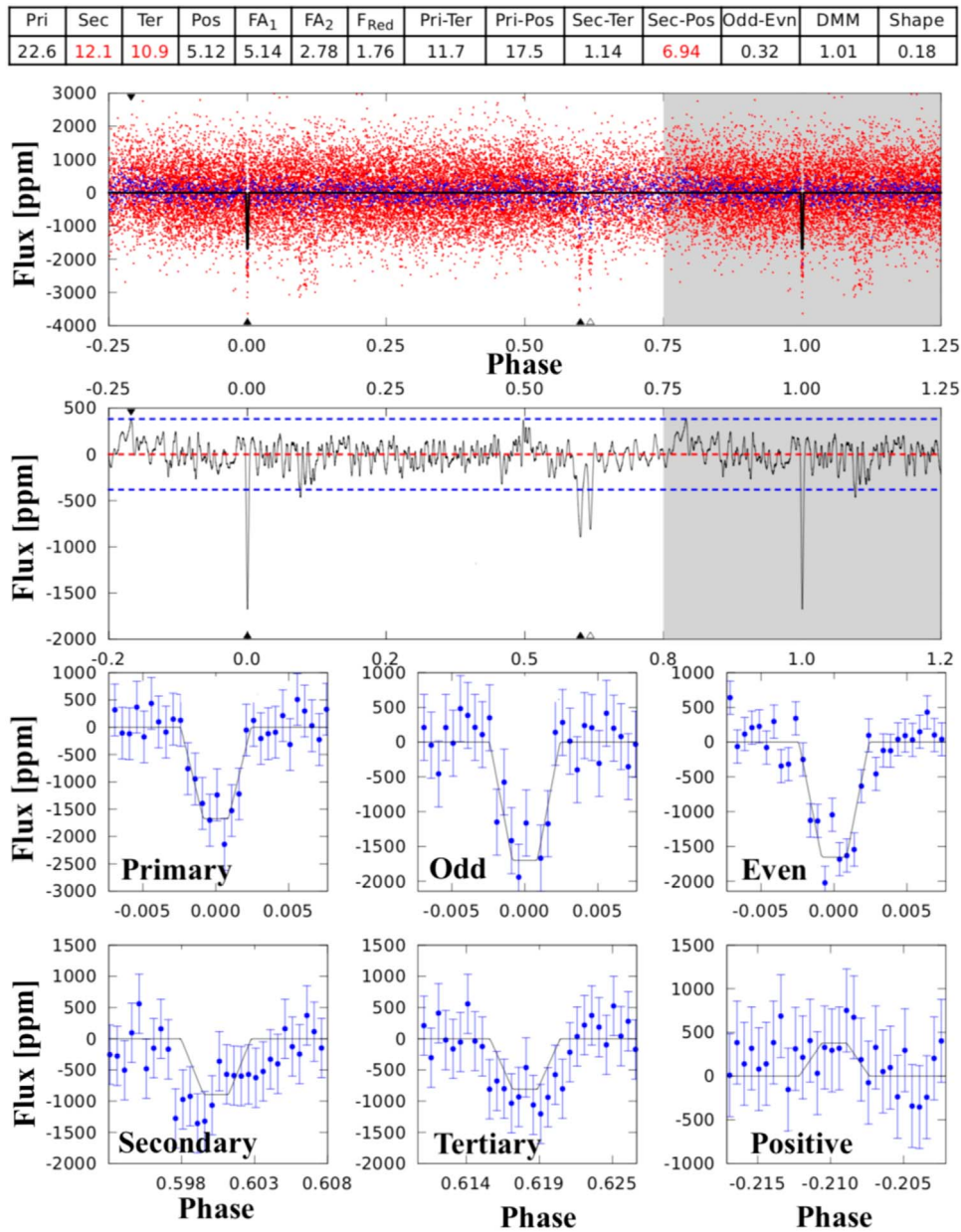
Pri	Sec	Ter	Pos	FA₁	FA₂	F_Red	Pri-Ter	Pri-Pos	Sec-Ter	Sec-Pos	Odd-Evn	DMM	Shape
22.6	12.1	10.9	5.12	5.14	2.78	1.76	11.7	17.5	1.14	6.94	0.32	1.01	0.18

Figure 7. Same as Figure 6 but for L 98-59 d. The significant secondary and tertiary features detected are transits of 175-01.

2.4. Follow-up Observations

We pursued ground-based follow-up of the three candidates to rule out potential sources of false positives and strengthen the evidence of their planetary nature. Our L 98-59 follow-up program was organized through the *TESS* Follow-up Observing Program (TFOP) Working Group (WG),[67] which facilitates follow-up of *TESS* candidate systems. The primary goal of the TFOP WG is to provide follow-up observations that will advance the achievement of the *TESS* Level One Science Requirement to measure masses for 50 transiting planets smaller than 4 Earth radii. A secondary goal of the TFOP WG is to foster communication and coordination for any science coming out of *TESS*. Our L 98-59 follow-up was conducted by three TFOP subgroups (SGs): SG-1, seeing-limited photometry; SG-2, reconaissance spectroscopy; and SG-3, high-resolution imaging.

2.4.1. Seeing-limited Photometry from the TFOP WG

Analysis of multiplanet systems from *Kepler* has shown that these have a higher probability of being real planets (e.g., Lissauer et al. 2012), lending credibility to the planetary nature of the transit events associated with L 98-59. However, the pixel scale of *TESS* is larger than *Kepler*'s (21″ for *TESS* versus 4″ for *Kepler*) and the point-spread function of *TESS* could be as large as 1′, both of which increase the probability of contamination by a nearby eclipsing binary (EB). For example, a deep eclipse in a nearby faint EB might mimic a shallow transit observed on the target star, due to dilution. Thus, it is critical to explore the potential contamination by relatively distant neighbors in order to confirm transit events detected on a *TESS* target.
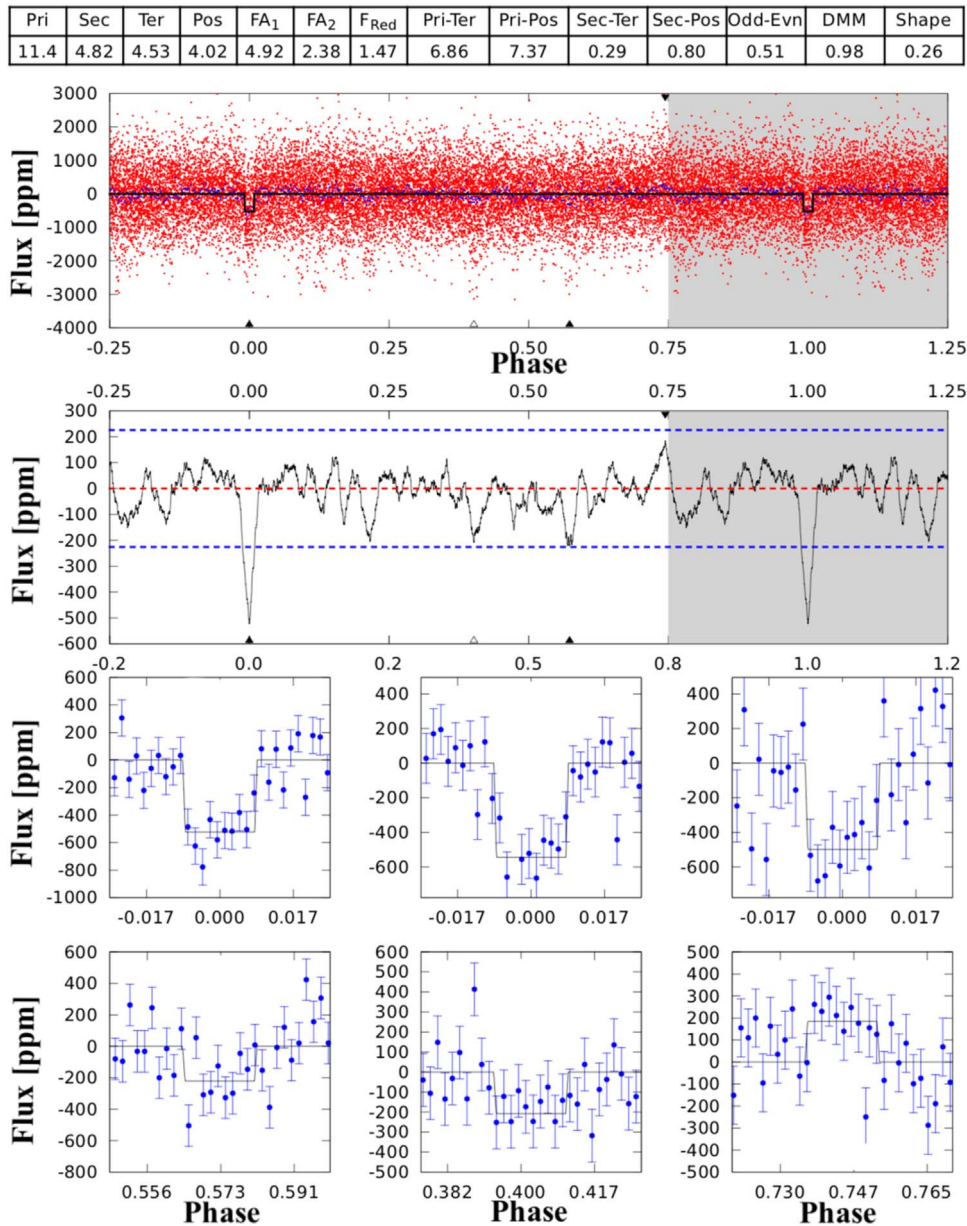
Pri	Sec	Ter	Pos	FA₁	FA₂	F_Red	Pri-Ter	Pri-Pos	Sec-Ter	Sec-Pos	Odd-Evn	DMM	Shape
11.4	4.82	4.53	4.02	4.92	2.38	1.47	6.86	7.37	0.29	0.80	0.51	0.98	0.26

Figure 8. Same as Figure 6 but for L 98-59 b.

To identify potential false positives due to variable stars such as EBs up to 2′.5 away from L 98-59, we made use of the TFOP SG-1. Specifically, we observed the target with ground-based facilities at the predicted times of the planet transits to search for deep eclipses in nearby stars at higher spatial resolutions. We used the *TESS* Transit Finder, which is a customized version of the Tapir software package (Jensen 2013), to schedule photometric time-series follow-up observations. The facilities we used to collect TFOP SG-1 data are the Las Cumbres Observatory (LCO) telescope network (Brown et al. 2013), SPECULOOS South Observatory (SSO; Burdanov et al. 2018; Delrez et al. 2018), MEarth-South telescope array (MEarth; Irwin et al. 2015), and Siding Spring Observatory T17 (SSO T17). Detailed observation logs are provided in Table 4.

We used the AstroImageJ software package (Collins et al. 2017) for the data reduction and the aperture photometry in most of these follow-up photometric observations. For the observations carried out at SSO, the standard calibration of the images and the extraction of the stellar fluxes were performed using the IRAF/DAOPHOT aperture photometry software as described in Gillon et al. (2013). The results are shown in Figures 13–15.

For all three planet candidates, we confirmed that the target star is the source of the transits and ruled out nearby EBs, which could mimic the transits. In addition, observations of L 98-59 c and d in different filters showed no chromatic dependence, which strengthens the hypothesis that the candidates are real planets. Our follow-up did detect a nearby EB at a separation of 54″ (TIC 307210845, Tmag = 16.042, i.e., ∼7 mag fainter than TIC 307210830, producing no detectable eclipses in the light curve of the latter), and we used deep exposures to confirm that it is not the origin of the L 98-59 b transits, providing a high level of confidence on the planetary nature of this candidate.
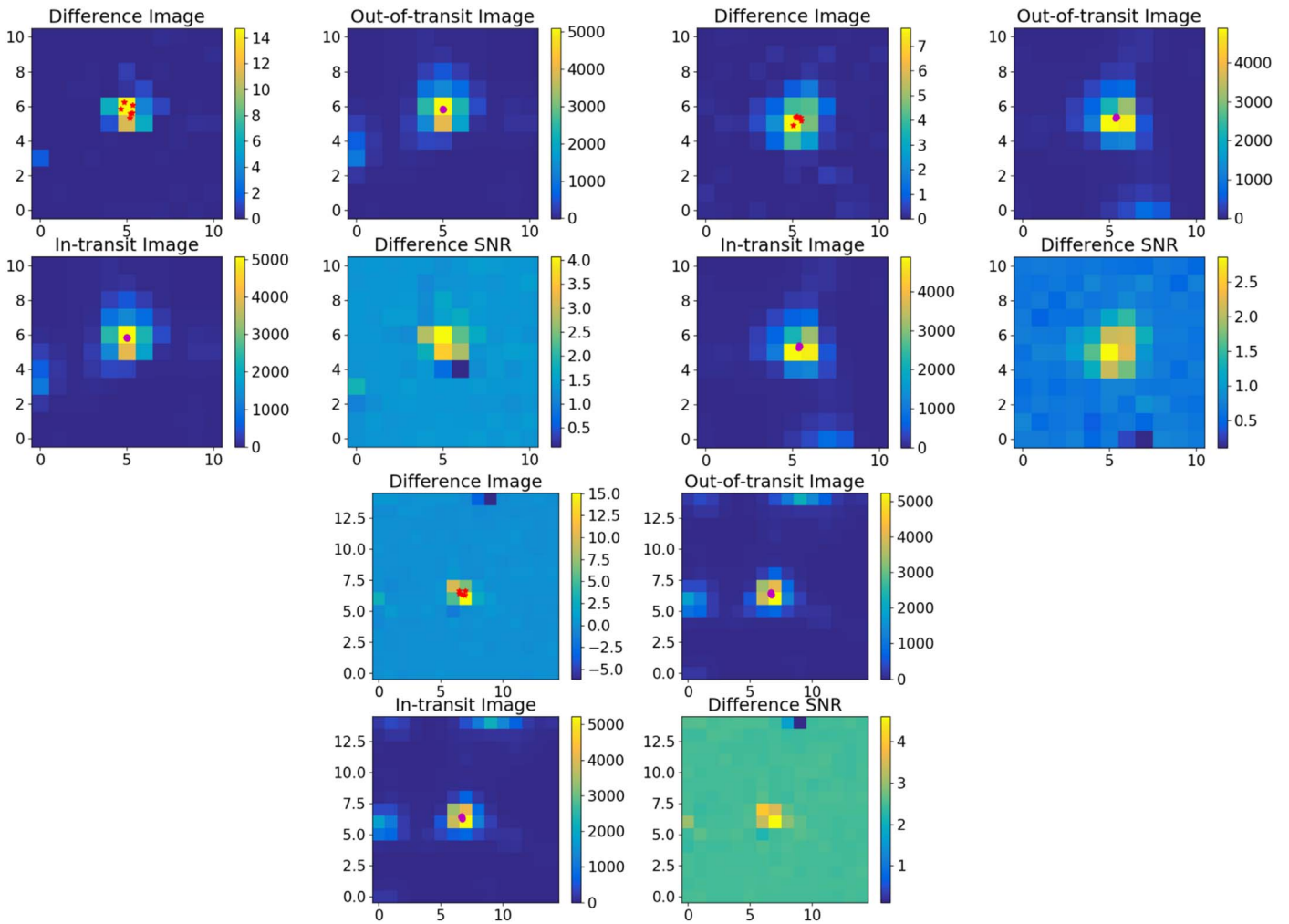
Figure 9. DAVE centroid analysis of L 98-59 c for Sector 2 (four upper left panels), Sector 5 (upper right panels), and Sector 8 (lower panels). The four panels shown are in the same format as in the Data Validation Report, i.e., the mean difference image (upper left), mean out-of-transit image (upper right), mean in-transit image (lower left), and signal-to-noise ratio of the mean difference image (lower right). The red circles and cyan stars represent the measured individual photocenter for each transit. We measure no significant photocenter shift between the difference and out-of-transit images, consistent with the transit signals originating from the target itself.

The measured transit depths revealed by follow-up transit photometry are consistent with the transit depths measured from *TESS*. The differences in the follow-up and *TESS* transit depth measurements (in terms of Rp/R^*) are listed in Table 5 as a function of wavelength, where we have included only the transits with scatter low enough to reasonably detect the events.

2.4.2. Reconnaissance Spectroscopy

To investigate the magnetic activity and rotation of L 98-59 and rule out spectroscopic binary companions, we obtained two epochs of optical spectra of L 98-59 on UT 2018 February 12[68] and on UT 2018 November 20 using the slicer mode with the CTIO HIgh ResolutiON (CHIRON) spectrograph (Tokovinin et al. 2013; $R \simeq 80,000$) on the Cerro Tololo Inter-American Observatory (CTIO)/ Small and Moderate Aperture Research Telescope System (SMARTS) 1.5 m telescope. CHIRON has a spectral range of 410–870 nm. We obtained one 7.5 minute exposure for the first epoch and 3×2.5 minute exposures for

the second observation, yielding a signal-to-noise ratio of roughly 13 in order 44 for both epochs. As described in Winters et al. (2018), we used an observed template of Barnard's Star to derive a radial velocity of -5.8 ± 0.1 km s^{-1} using the TiO molecular bands at 7065–7165 Å.[69] Our analyses of the spectra reveal no evidence of double lines. We see negligible rotational broadening ($v \sin i = 0.0 \pm 1.9$ km s^{-1}) and do not see Hα in emission, providing evidence that the star is inactive and not host to unresolved, close-in, stellar companions. We are also able to rule out the presence of a brown dwarf companion to the host star. The radial-velocity difference between the two observations, separated in time by roughly nine months, is 53 ± 52 m s^{-1}. For comparison, a 13 Jupiter-mass companion in a circular, nine-month period would induce a velocity semiamplitude of 863 m s^{-1} on this star. This semiamplitude is eight times larger than our velocity uncertainty and would have been readily detectable. Thus, it is highly unlikely that there is a low-mass stellar or brown

---

[68] The first epoch of spectroscopic data was obtained as part of the M dwarf spectroscopic program described in Winters et al. (2019), before *TESS* began observations.

[69] We note that the total uncertainty on the systemic velocity should include the 0.5 km s^{-1} uncertainty on the Barnard's Star template velocity.
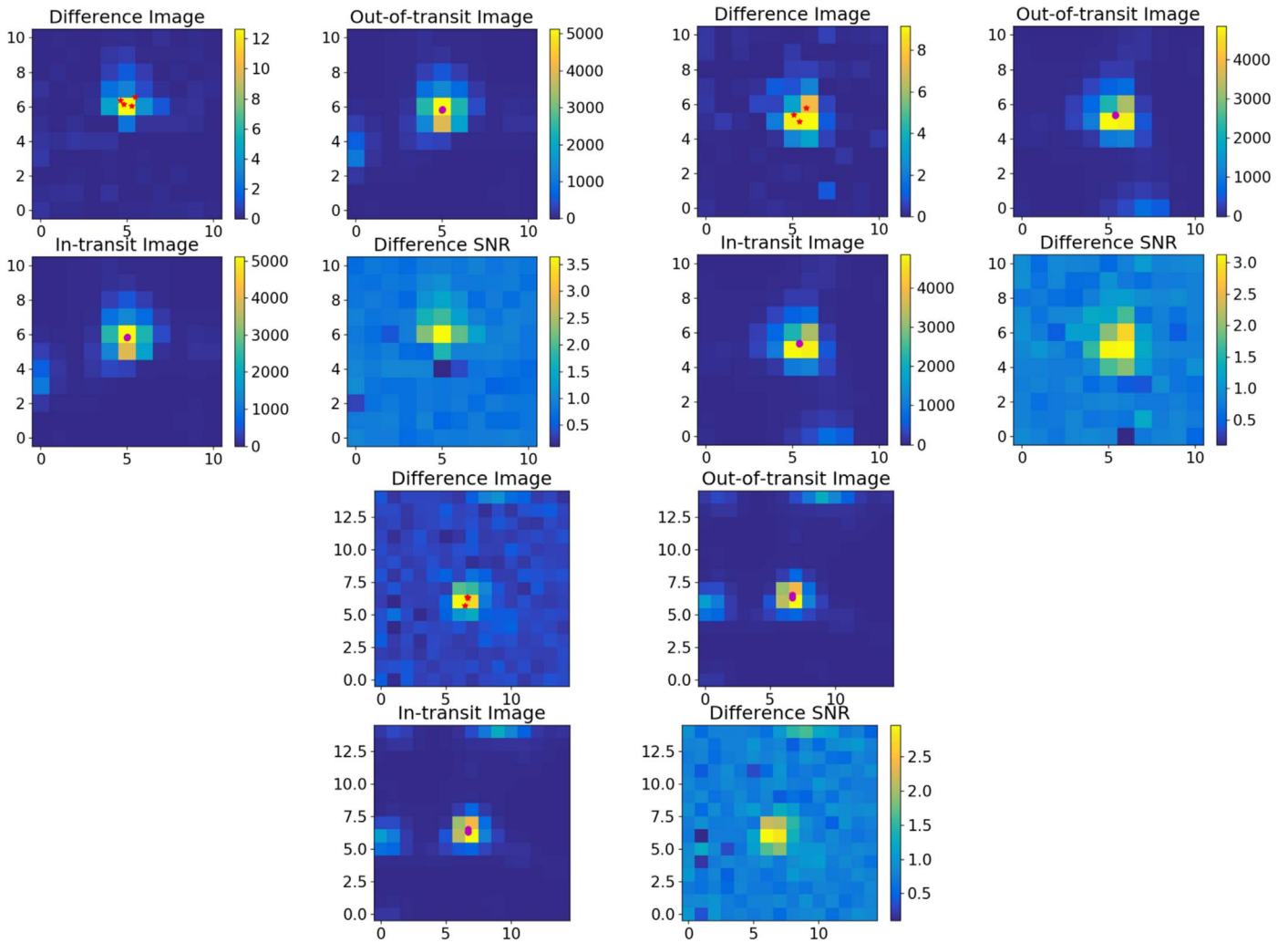
Figure 10. Same as Figure 9 but for L 98-59 d.

dwarf companion around L 98-59 at periods shorter than nine months.

We note, as well, that the trigonometric distance of 10.623 ± 0.003 pc from the *Gaia* second data release is in agreement with the photometric distance estimate of 12.6 ± 1.9 pc reported in Winters et al. (2019). Undetected equal-luminosity companions would contribute light to the system, making the system overluminous and resulting in an underestimated photometric distance estimate. Because the two distances are in agreement, this lends further support to the host star being a single star.

We also placed L 98-59 on an observational Hertzsprung–Russell color–magnitude diagram (blue star; see Figure 16). Because it is not elevated above the main sequence or among the blended photometry binary sequence (red points), even more strength is given to the argument of this star being single.

In addition, we obtained a near-IR spectrum of L 98-59 on 2018 December 22 with the Folded-port InfraRed Echellete (FIRE) spectrograph (Simcoe et al. 2008) on the 6.5 Baade Magellan telescope at Las Campanas observatory. FIRE covers the 0.8–2.5 μm band with a spectral resolution of $R = 6000$. The target was observed under favorable conditions, with an average seeing of $\sim 0''\!.6$. L 98-59 was observed twice in the ABBA nod patterns at 40 s integration time for each frame

using the $0''\!.6$ slit. Reductions and telluric corrections, using the nearby A0V standard HIP 41451, were completed with the FIREhose IDL package. We derived stellar parameters following the empirical methods derived by Newton et al. (2015). For L 98-59, we infer: $T_{\rm eff} = 3620 \pm 74$ K, $R_{\rm star} = 0.37 \pm 0.027 R_\odot$, and $L = 0.021 \pm 0.004 L_\odot$, consistent with the SED analysis.

2.4.3. High-resolution Imaging

Photometric contamination from nearby sources can result in various false-positive scenarios (e.g., background eclipsing binaries) and can bias the measured planetary radius from photometric analysis (see, e.g., Ciardi et al. 2015; Furlan & Howell 2017; Ziegler et al. 2018). In this work, we use several high-resolution images to tightly constrain the possible background sources and companion stars present near L 98-59. Previous speckle observations of the target were collected with Gemini/DSSI on 2018 March 31 as part of the M dwarf speckle program described in Winters et al. (2019). Once the candidate planets in this system had been identified by *TESS*, we collected additional speckle images with Gemini/DSSI (Horch et al. 2011) on 2018 November 1 and AO images with VLT/NaCo on 2019 January 28. Both epochs of Gemini/DSSI data are collected simultaneously through the *R*- and *I*-band
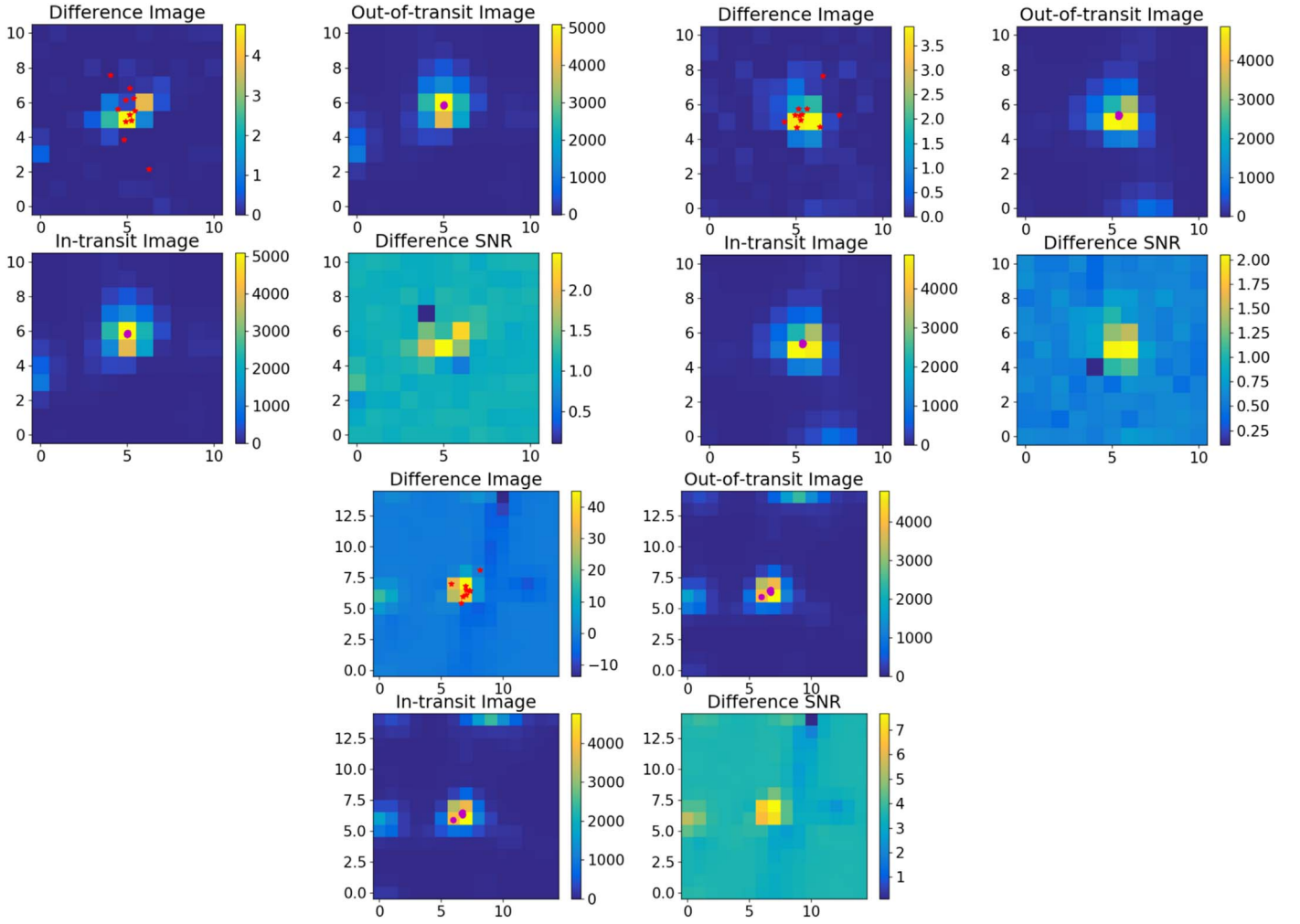
Figure 11. Same as Figure 9 but for L 98-59 b.

Table 3
Photocenter Analysis of the Three Planet Candidates

Parameter	Row (pixels)	Column (pixels)
L 98-59 b		
Out-of-transit image centroid	338.83 ± 0.02	664.01 ± 0.01
Difference image centroid	338.34 ± 1.39	664.04 ± 0.55
Offset	−0.49 ± 1.39	0.03 ± 0.55
Offset/σ	0.35	0.05
L 98-59 c		
Out-of-transit image centroid	338.83 ± 0.02	664.01 ± 0.01
Difference image centroid	338.76 ± 0.31	664.11 ± 0.24
Offset	−0.07 ± 0.31	0.1 ± 0.24
Offset/σ	0.23	0.42
L 98-59 d		
Out-of-transit image centroid	338.93 ± 0.02	664.02 ± 0.02
Difference image centroid	339.27 ± 0.21	664.06 ± 0.34
Offset	0.34 ± 0.21	0.04 ± 0.34
Offset/σ	1.62	0.12

filters (692 nm and 880 nm respectively), while the VLT/NaCo data are collected in the Brγ filter. At 0″.5 from the host, these data rule out companions 5.0, 6.6, and 5.8 mag fainter than the host star in the R, I, and Brγ bands, respectively. The 5σ contrast curves for each of these observations are presented in Figure 17.

Due to the high proper motion of the target (354 mas yr^{-1}), the target undergoes significant motion even over the relatively modest time baseline of these observations. The on-sky position of the target is displaced by 338 mas between the observations on 2018 March 31 and 2019 January 28. This motion is significantly more than the PSF width in the high-resolution images, and we are therefore able to rule out the presence of stationary background objects within ∼6 mag of the host at any separation: any background objects obscured by the target in the first observation would be clearly visible in the final observation and vice versa. The motion of the target is demonstrated in Figure 17. These data also allow tight constraints to be placed on the presence of comoving companions beyond ∼150 mas (=1.6 au at the distance of this target). An object with ΔBrγ ∼ 6 mag and at the distance of L 98-59 would have a mass of ∼75M_J at an age of 10 Gyr (Baraffe et al. 2003),[70] and we can therefore rule out any stellar companions to this host with a projected separation greater than 1.6 au, while stellar companions closer than this could be easily detected in radial-velocity data with a sufficient baseline.

Overall, the follow-up efforts demonstrate that there are tentative transit detections of the various candidates from the ground, but it is difficult to confirm them because they are all

---

[70] Given the difficulty in estimating M-dwarf ages, we use an age of 10 Gyr so as to calculate a conservative mass limit.
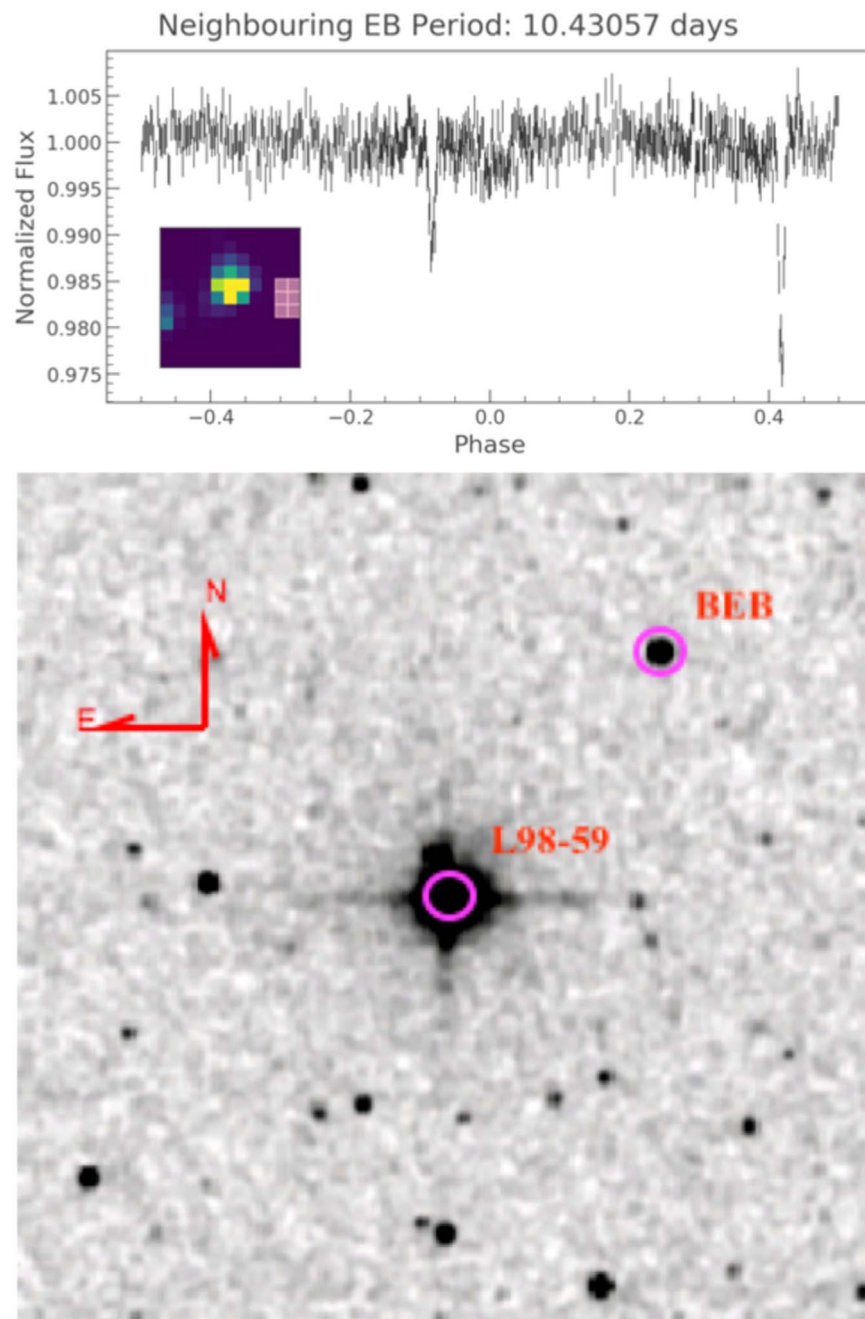
Figure 12. Upper panel: lightkurve analysis of the nearby field star 2MASS 08181825-6818430 showing that it is a background eclipsing binary (BEB) with a period of 10.43 days. The inset panels shows the pixel mask used to extract the light curve of the field star (near the right edge of the aperture) not physically associated with the target star. Lower panel: $4' \times 4'$ (the size of the *TESS* aperture) 2MASS *J*-band image showing the position of the background eclipsing binary (BEB).

shallow events. More importantly, none of these detections were identified as eclipsing binary scenarios (either on the host star or on nearby stars), supporting the planetary nature of the three transit candidates.

3. Discussion

Our light-curve and false-positive analyses, follow-up observations, and the multiplicity of the system provide strong evidence that the detected transit signals are planetary in nature. We consider the planets L 98-59 b, c, and d to be a validated system of terrestrial planets orbiting a very nearby, bright M dwarf. Here we explore additional properties of the system to

place constraints on the planet masses, orbital dynamics, and evolution, and discuss their potential for future characterization.

3.1. Planet Mass Constraints

In the absence of radial-velocity measurements, we placed constraints on the masses of the planets using the forecaster package for probabilistic mass forecasting (Chen & Kipping 2017). From the mean and standard deviation of each planet's radius, we generated a grid of 5000 masses within the entire mass range of the conditioned model, which spans dwarf planets to high-mass Jovians, and sampled 50,000 times from a truncated normal distribution. For each sampled radius,

Table 4
Observation Log

L 98-59 Planet	Date (UTC)	Telescope[a]	Filter	ExpT (s)	Exp (N)	Dur. (minutes)	Transit Coverage	Aperture (arcsec)	FWHM (arcsec)
b	2018 Oct 19	LCO-SSO[b]	r'	120	41	147	Ingr.+71%	3.89	2.21
	2018 Nov 11	SSO-Europa	r'	15	764	315	Full	5.25	4.53
	2018 Nov 11	LCO-CTIO-1	i'	25	120	154	Full	5.83	3.49
	2018 Nov 18	LCO-SAAO-0.4[b]	i'	70	125	175	Full	9.14	7.03
	2018 Nov 20	LCO-CTIO-1	r'	30	146	178	Full	3.89	2.20
	2018 Nov 29	LCO-CTIO-1	r'	30	186	223	Full	5.83	3.56
	2018 Dec 7	SSO-Io	r'	15	998	415	Full	5.60	4.06
	2019 Jan 26	LCO-SAAO-1[b]	r'	12	88	234	Full	3.89	3.08
c	2018 Oct 16	LCO-CTIO-1	i'	20	63	70	Ingr.+30%	4.27	2.01
	2018 Oct 22[b]	SSO-T17	clear	30	122	86	Ingr.+77%	7.10	2.40
	2018 Nov 11	SSO-Europa	r'	15	764	315	Full	5.25	4.53
	2018 Nov 22	MEarth	RG715	45	1682	380	Full	20.16	8.00
	2018 Dec 25	LCO-SSO-1	i'	22	108	113	Full	5.05	1.89
	2019 Jan 20	LCO-CTIO-1	g'	100	85	197	Full	6.22	2.75
	2019 Jan 20	LCO-CTIO-1	zs	30	170	197	Full	9.36	4.43
d	2018 Nov 7	LCO-CTIO-0.4	i'	70	119	170	Full	6.85	4.48
	2018 Nov 22	LCO-CTIO-1[b]	i'	25	108	113	Full	6.22	5.05
	2018 Nov 22	MEarth	RG715	45	1682	380	Full	20.16	8.00
	2019 Jan 13	LCO-CTIO-0.4	i'	14	143	73	Full	5.14	2.32
	2019 Jan 20	LCO-CTIO-1	r'	30	132	151	Full	6.22	2.89
	2019 Jan 28	LCO-CTIO-1	g'	50	153	223	Full	7.78	2.35

Notes.
[a] Telescopes: LCO-SSO-1: Las Cumbres Observatory—Siding Spring (1.0 m), LCO-CTIO-1: Las Cumbres Observatory—Cerro Tololo Inter-American Observatory (1.0 m), LCO-CTIO-0.4: Las Cumbres Observatory—Cerro Tololo Inter-American Observatory (0.4 m), LCO-SAAO-1: Las Cumbres Observatory—South African Astronomical Observatory (1.0 m), LCO-SAAO-0.4: Las Cumbres Observatory—South African Astronomical Observatory (0.4 m), SSO-Europa: SPECULOOS South Observatory—Europa (1.0 m), SSO-Io: SPECULOOS South Observatory—Io (1.0 m), SSO-T17: Siding Spring Observatory—T17 (0.4 m), MEarth: MEarth-South telescope array (0.4 m × 5 telescopes.)
[b] Observations not shown in Figures 13–15 due to intrinsically high scatter in the light curve and/or because they were a deep exposure search for eclipsing binaries in nearby stars.

forecaster computes a vector of probabilities given each element in the mass grid and a randomly chosen set of hyperparameters from the hyperposteriors of the model (which include transition points and intrinsic dispersion in the mass–radius relation). From this vector, the package returns the median mass and $\pm 1\sigma$ values. From the calculated radius values of 0.8 [0.05] $R_\oplus$ (L 98-59 b), 1.35 [0.07] $R_\oplus$ (L 98-59 c), and 1.57 [0.14] $R_\oplus$ (L 98-59 d), we determined mass values of 0.5 [+0.3, −0.2] $M_\oplus$, 2.4 [+1.8, −0.8] $M_\oplus$, and 3.4 [+2.7, −1.4] $M_\oplus$, respectively. The large errors on these values suggest that better constrained radii from continued follow-up observations, combined with precise radial-velocity measurements, are necessary to constrain the true masses. We note that given the brightness of the host star, the L 98-59 planets should be great targets for mass measurements to establish the M–R relation for M-dwarf planets. Using the forecaster masses, the expected radial-velocity semiamplitude, K, for the three planets are 0.54, 2.22, and 2.48 m s^{-1} for L 98-58 b, L 98-58 c, and L 98-58 d, respectively, the outer two comparable to the amplitude of the measured radial-velocity signal produced by, e.g., GJ 581 b (Mayor et al. 2009) and Proxima Centauri b (Anglada-Escudé et al. 2016).

3.2. Dynamical Stability and Transit Timing Variations

3.2.1. Long-term Stability

To examine the long-term dynamical stability and orbital evolution of the L 98-59 planets, we integrated the system using Rebound (Rein & Spiegel 2015) for 1 million orbits of the outer planet ($P = 7.45$ days). We used two sets of initial conditions—planets on circular orbits and on eccentric orbits with $e = 0.1$—and start all integrations with randomly selected initial arguments of periastron. Given the large uncertainties on the forecaster masses, we also tested the dynamical stability for two sets of planetary masses: best-fit masses (i.e., 0.5 $M_\oplus$, 2.4 $M_\oplus$, and 3.4 $M_\oplus$ for L 98-58 b, L 98-58 c, and L 98-58 d, respectively), and best-fit+1σ masses (i.e., 0.58 $M_\oplus$, 4.2 $M_\oplus$, and 6.1 $M_\oplus$ for L 98-58 b, L 98-58 c, and L 98-58 d, respectively). Overall, we performed 1000 numerical simulations for each set of planetary masses, using the IAS15 nonsymplectic integrator (Rein & Spiegel 2015) with a time step of 0.01 times the orbit of the inner planet (i.e., about 30 minutes).

Our simulations show that for initially circular orbits, the semimajor axes and eccentricities do not exhibit extreme variations, the system does not exhibit chaotic behavior for the duration of the numerical integrations for either set of planet masses, and the orbits remain practically circular (Figure 18). In contrast, for initially eccentric orbits with $e = 0.1$, the system becomes unstable in half of our simulations (with randomly selected initial arguments of periastron), both for the best-fit and the best-fit+1σ planet masses (Figure 19). Thus, we consider orbits with nonnegligible eccentricity as unlikely. This is consistent with other compact multiplanet systems where the orbital eccentricities are typically on the order of a few percent (e.g., Hadden & Lithwick 2014) and is in line with the L 98-59
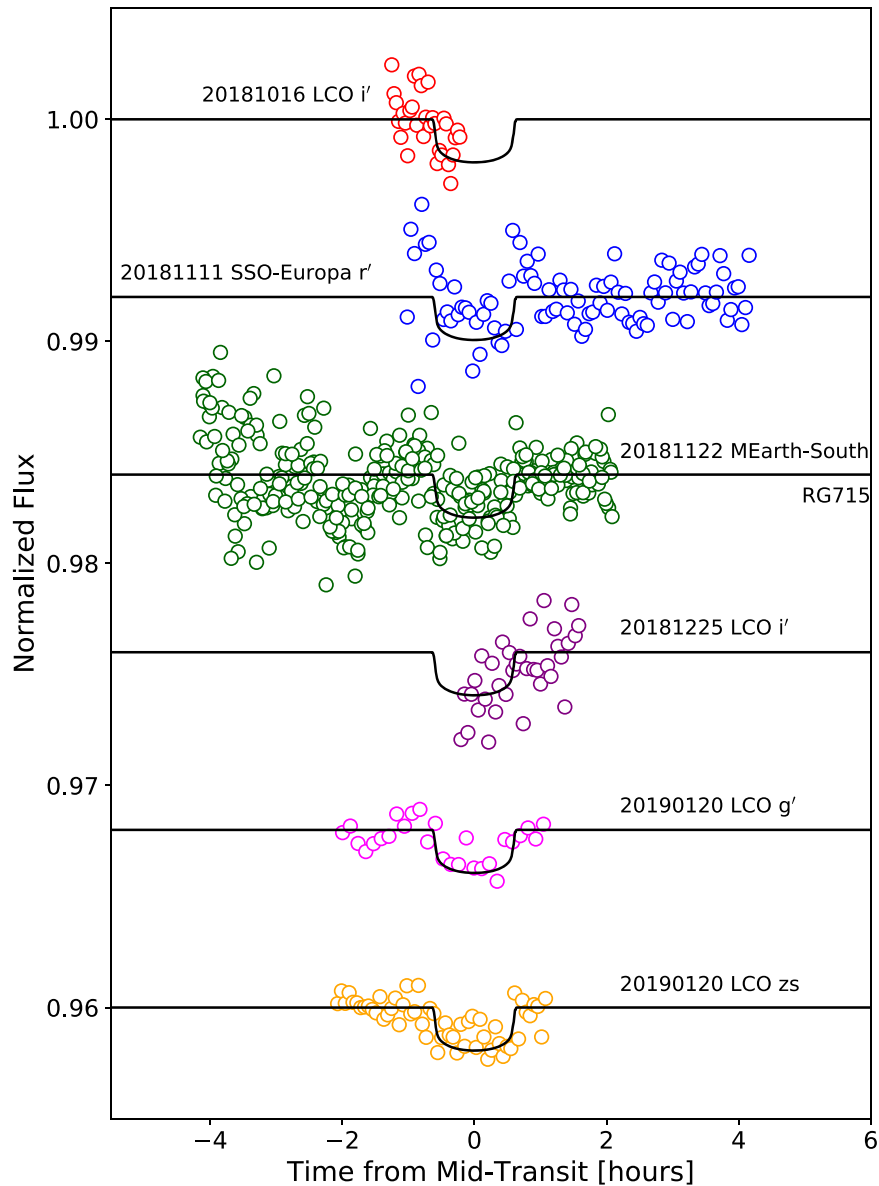
Figure 13. Ground-based follow-up observations of L 98-59 c. The date, facility, and filter used for each observation is marked, and each data set is offset for clarity. The black line represents the transit model based on the *TESS* data.

planets being close to but not in resonance (where the orbits may potentially be eccentric; e.g., Charalambous et al. 2018).

Inspired by the closely spaced multiplanet systems discovered by *Kepler* (Muirhead et al. 2015) and other surveys (e.g., Gillon et al. 2017), we also explored the possibility of a fourth, nontransiting planet having a dynamically stable orbit in between L 98-59 c and L 98-59 d such that the four planets would form a near-resonant chain of 5:8:12:16 period commensurability similar to, e.g., TRAPPIST-1 (Gillon et al. 2017). As an example, we tested a planet with a mass of 2.5 $M_\oplus$ and a 5.7 day orbital period ($\approx$1.55 and $\approx$0.77 times the period of L 98-59 c and L 98-59 d, respectively), again for two cases of (a) initially circular orbits and (b) initially eccentric orbits with $e = 0.1$. For simplicity, we only used the best-fit masses for the three planet candidates. The system is dynamically stable in case (a) for the duration of the integrations (Figure 20, upper panel) and becomes unstable within a few thousand orbits of the outer planet for case (b). Thus, such a hypothetical planet is potentially possible if on a

circular orbit. Overall, while a comprehensive dynamical analysis for the presence of additional planets is beyond the scope of this work, we will continuously monitor the system as data from future *TESS* sectors become available.

3.2.2. Transit Timing Variations

If detected, deviations in the times of transits from a linear ephemeris can be a powerful method to constrain the masses and orbital eccentricities of planets in multiplanet systems (e.g., Agol et al. 2005). We measured transit times for each individual transit using two different methods. First, we folded the transits on a linear ephemeris, fitting a transit model using the models of Mandel & Agol (2002). Next, we measured the time of each individual transit by, for each transit, sliding this model across a grid of potential transit midpoints with a time resolution of one second, and measuring the likelihood of each transit fit at each grid point. We then found the maximum-likelihood transit time and a 68% confidence interval on the
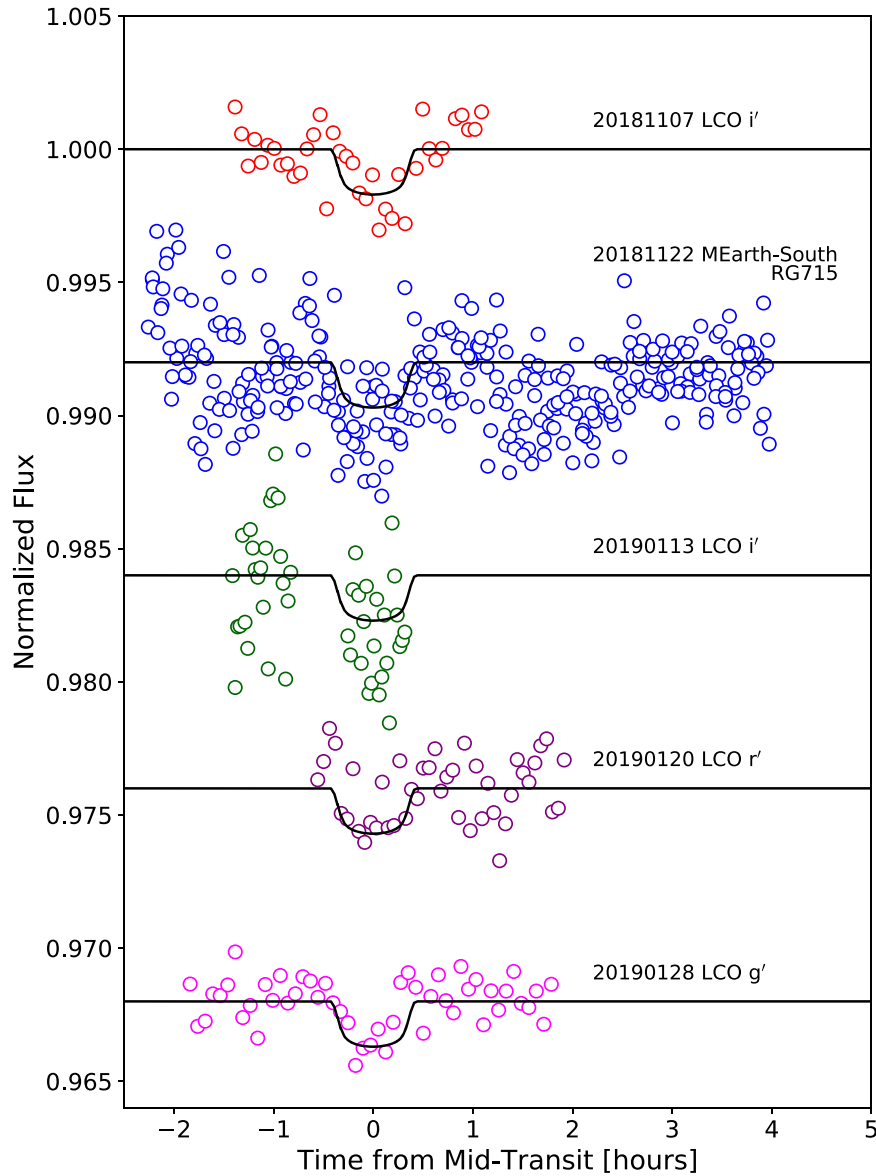
Figure 14. Same as Figure 13 but for L 98-59 d.

same. The ability to measure TTV signals depends sensitively on our ability to measure precise transit times. For L 98-59 b, the scatter in measured transit times, suggestive of the ultimate transit timing precision we measure, is 5.1 minutes. For L 98-59 b, this is 2.1 minutes, and for L 98-59 d, 1.2 minutes. Our analysis showed that a linear ephemeris is sufficient to reproduce the transit times of the three planet candidates detected in Sector 2. We found no evidence for TTVs, and no further constraints can be placed on the parameters of the system beyond those already provided by dynamical stability considerations. Given that L 98-59 will be observed in 7 of the 13 sectors that comprise the first year of the *TESS* mission (Mukai & Barclay 2017; Sectors 2, 5, 8, 9, 10, 11, and 12), here we examine how continued *TESS* observations would affect the transit timing analysis of the system.

Specifically, we simulated continued observations following the nominal *TESS* schedule, assuming a linear ephemeris for future transits and that every planned sector will be observed as scheduled. We then used the TTVFast package (Deck et al. 2014) to calculate predicted transit times for the three planets in

various orbital configurations consistent with the current data and examine what can be ruled out by the data by the end of the mission.

The two outer planets (L 98-59 c and d) are close to first-order period commensurability (period ratio of 2.02), whereas the inner planet is not near a first-order resonance with either of the other planets (1.64 period ratio between L 98-59 b and L 98-59 c, and 3.31 period ratio between L 98-59 b and L 98-59 d). Thus, the expected TTV signal for the former planet pair is stronger compared to that for the latter planet pair. Indeed, even for eccentricities of $\sim$0.1, the expected TTV amplitude for the innermost planet is $\sim$90 s, notably smaller than the observed precision on the measured times of transit. To evaluate the potential for measuring TTVs for the outer two planets, we performed numerical simulations of the system for the first year of the *TESS* mission (using TTVFast), thus covering all sectors it will be observed in. We allowed the planet eccentricities to vary, and assumed the maximum-likelihood masses listed in Section 3.1. Adopting a transit timing precision of 1–2 minutes, we found that significant TTVs could be detected if the
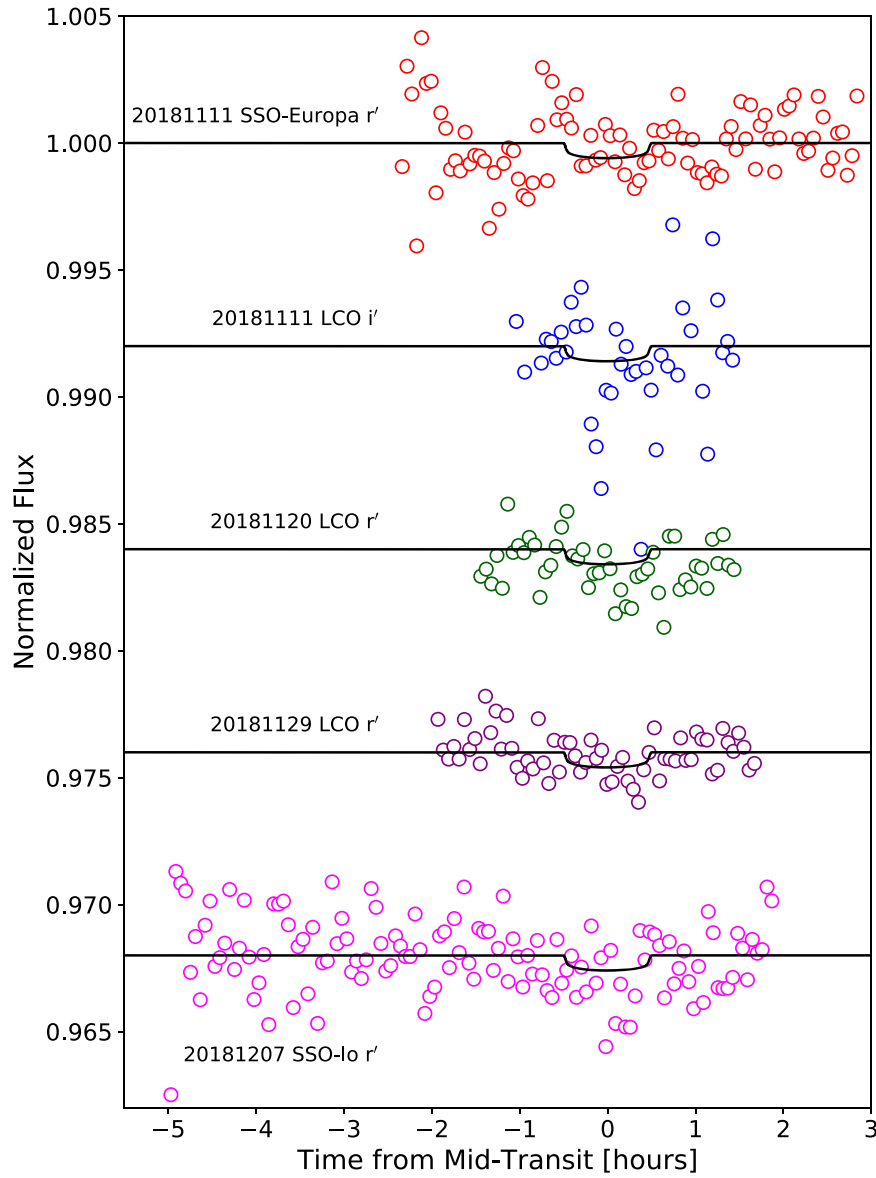
Figure 15. Same as Figure 13 but for L 98-59 b.

Table 5
Ground-based Follow-up R_p/R_* Less *TESS* R_p/R_* as a Function of Wavelength

TOI	Date Obs	Filter (Observatory)	R_p/R_* Less *TESS* R_p/R_*
L 98-59 b	UT 2018 Nov 20	Sloan r' (LCO)	$-0.0008^{+0.0054}_{+0.0085}$
L 98-59 b	UT 2018 Nov 29	Sloan r' (LCO)	$0.0018^{+0.0039}_{-0.0045}$
L 98-59 c	UT 2019 Jan 20	Sloan g' (LCO)	-0.0033 ± 0.003
L 98-59 c	UT 2018 Nov 22	RG715 (MEarth)	-0.0007 ± 0.002
L 98-59 c	UT 2019 Jan 20	Sloan z' (LCO)	-0.0056 ± 0.0028
L 98-59 d	UT 2019 Jan 28	Sloan g' (LCO)	$0.0072^{+0.0078}_{-0.0064}$
L 98-59 d	UT 2019 Jan 20	Sloan r' (LCO)	$-0.003^{+0.01}_{-0.012}$
L 98-59 d	UT 2018 Nov 7	Sloan i' (LCO)	$0.0072^{+0.0088}_{-0.0072}$
L 98-59 d	UT 2018 Nov 22	RG715 (MEarth)	$0.0104^{+0.0044}_{-0.0043}$

eccentricities of the outer two planets were larger than ∼0.03 (as shown in Figure 21).

Overall, as multiplanet systems typically have orbital eccentricities of a few percent (Hadden & Lithwick 2016), it is unlikely that *TESS* will reveal timing variations for this system during its primary mission; doing so would suggest either anomalously large eccentricities (which are unlikely based on dynamical stability consideration) or significantly
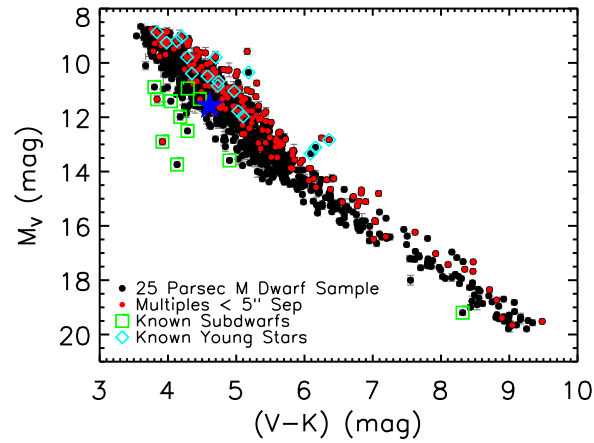
Figure 16. Observational Hertzsprung–Russell diagram. The sample of 1120 M dwarf primaries within 25 pc from Winters et al. (2019) is plotted as black points. L 98-59 is noted as a blue star. For comparison, known close multiples with separations less than $5''$ having blended photometry (red points), known cool subdwarfs (open green squares), and known young objects (open cyan diamonds) are noted. Error bars are shown in gray and are smaller than the points, in most cases.
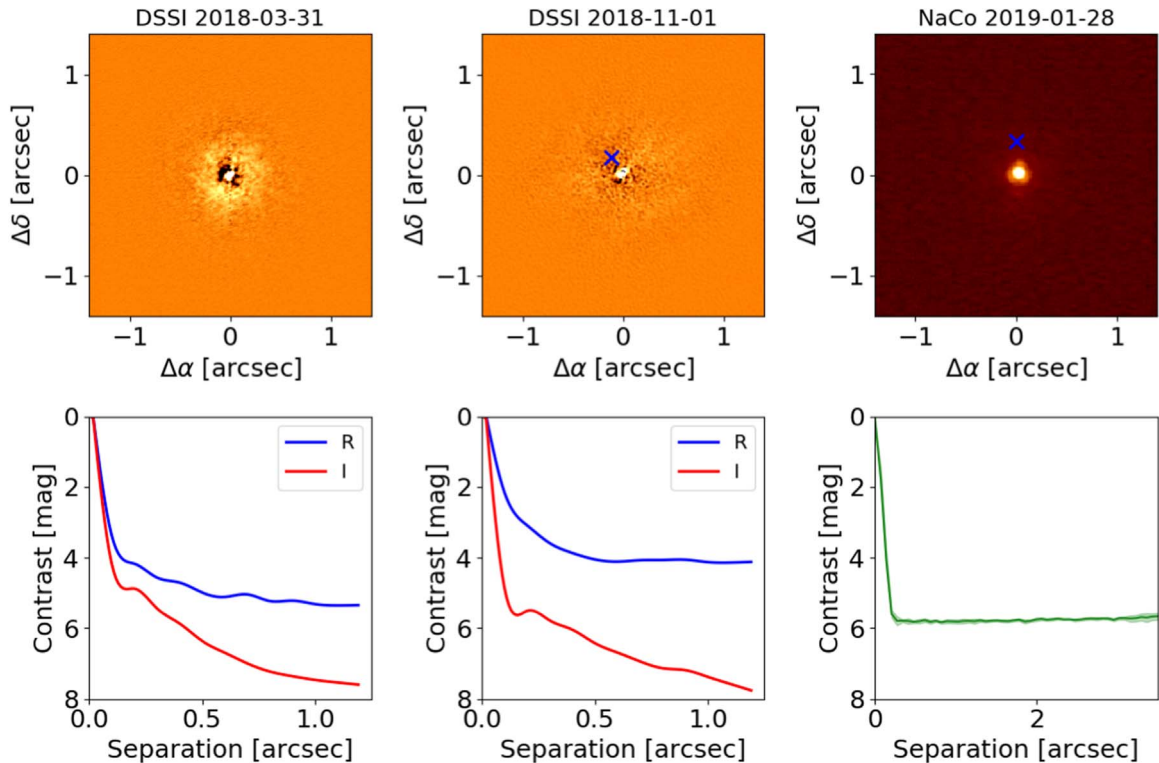
Figure 17. Top: high-resolution images of the target at each epoch. In the center and right panels, the blue cross indicates the position of the target on UT 2018 March 31, when the first Gemini/DSSI data set was collected, and we show only the *I*-band images here. No companions are detected here or anywhere in the field of view in any of the images. Only the central portion of the NaCo image is shown. Bottom: 5σ sensitivity to companions as a function of separation from the host star, for each data epoch. Red and blue lines indicate the Gemini/DSSI *R*- and *I*-band observations, respectively, which have central wavelengths of 692 and 880 nm.

larger planet masses/densities in this system relative to planets with similar radii in other systems.

To explore TTVs using an alternative software framework, we also used the TTV2Fast2Furious package (Hadden et al. 2018) to project the expected TTV signals of the planets through Sector 12, again adopting the forecaster masses and, for simplicity, assuming circular orbits. Similar to the TTVFast analysis described above, our results show that it is unlikely TTVs are measurable for this system during the *TESS* prime mission—the maximum TTV amplitudes are 0.09 minutes for

L 98-59 b, 0.17 minutes for L 98-59 c, and 0.56 minutes for L 98-59 d (see Figure 22).

Following the approach described in Hadden et al. (2018), we also used TTV2Fast2Furious to project the precision of mass constraints derived from future *TESS* transit timing measurements. Planet mass constraints derived from TTVs depend on the precision of transit time measurements, and we adopt the measured scatter in the transit time measurements taken through Sector 2, $\sigma_{t_{L98-59c}} = 2.1$ minutes and $\sigma_{t_{L98-59d}} = 1.2$ minutes. The planets' masses are expected to be
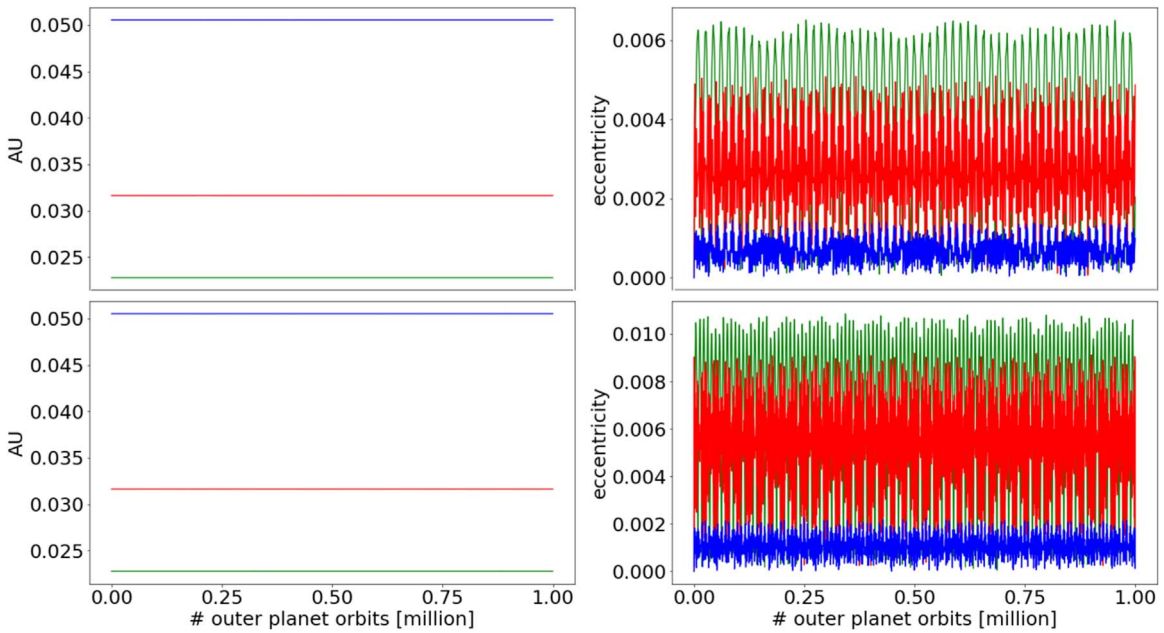
Figure 18. The evolution of the planets' semimajor axes (left panels) and eccentricities (right panels) for the corresponding best-fit (upper panels) and best-fit+1σ (lower panels) masses for 1 million orbits of the outer planet (L 98-59 d), and assuming initially circular orbits. The orbital elements do not experience drastic variations, and the system is dynamically stable for the duration of the integrations.
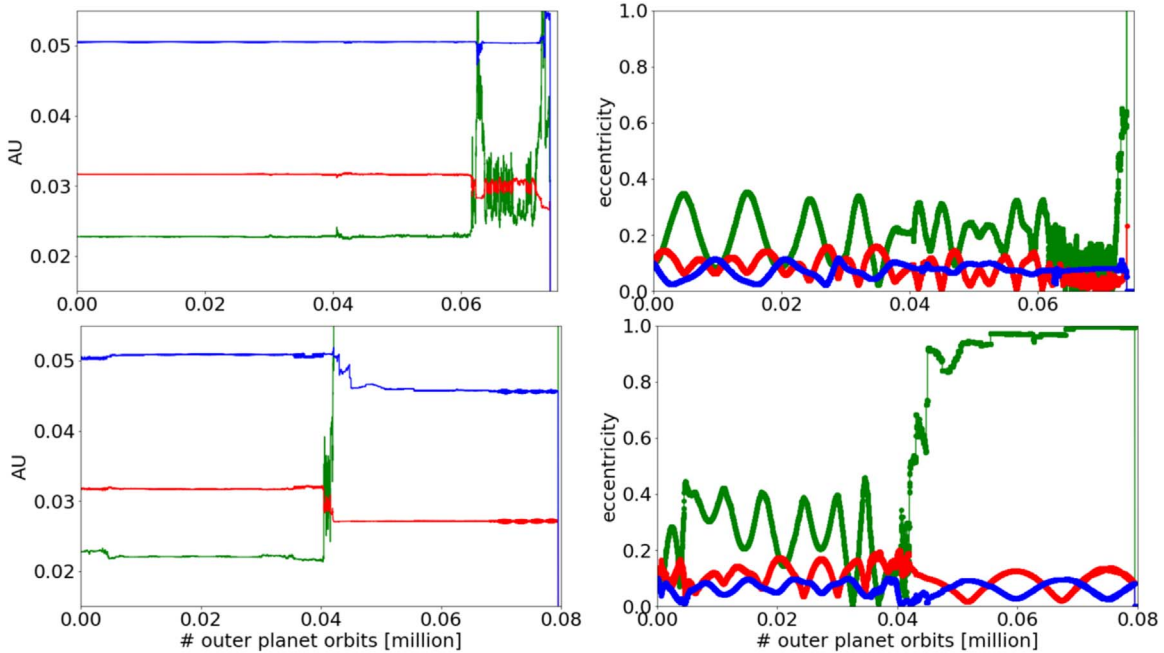
Figure 19. Same as Figure 18 but for planets on initially eccentric orbits with $e = 0.1$. The system becomes dynamically unstable within a few thousand orbits of the outer planet in half of our simulations, both for the best-fit and for the best-fit $+1\sigma$ masses.

constrained with precisions of $\sigma_{m,\text{L98-59c}} = 13.1\ M_\oplus$ and $\sigma_{m,\text{L98-59d}} = 5\ M_\oplus$ with transit timing data through Sector 12.[71]

With three sectors of data available for this system at the time of writing (Sectors 2, 5, and 8), there is at present no evidence for TTVs. In line with the predictions of the previous paragraph, there is no significant mass constraint beyond what is given from plausible compositions of terrestrial planets. We use TTVFast to compare maximum-likelihood dynamical models of the orbits of the planets, assuming the masses listed in Section 3.1. We also repeat this procedure holding the masses fixed at four times this nominal value, which would imply a density of $\sim$20 g cm^{-3}. In both scenarios, there is a dynamical model that fits the observed transits equally well. This is partly due to the large gaps in the

---

[71] If the planets are restricted to circular orbits in the TTV model, e.g., under the assumption that eccentricities are damped away by tidal dissipation, the mass–eccentricity degeneracy (e.g., Lithwick et al. 2012) is removed, and the measured TTV signals therefore place tighter constraints on the planet masses. In particular, if the TTV model is restricted to circular orbits, the mass measurement precisions of $\sigma_{m,\text{L98-59c}} = 3.4 M_\oplus$ and $\sigma_{m,\text{L98-59d}} = 2.1 M_\oplus$ are projected.

21

Figure 20. Same as Figure 18 but for the three known planets (with best-fit masses) and a hypothetical fourth planet in between L 98-59 c and L 98-59 d, with a mass of 2.5 $M_\oplus$ and a period of 5.7 days. All four planets are on initially circular orbits (upper panel) or on initially eccentric orbits with $e = 0.1$ (lower panels). While the system is dynamically stable for the duration of the integrations in the former case, it quickly becomes unstable in the latter.
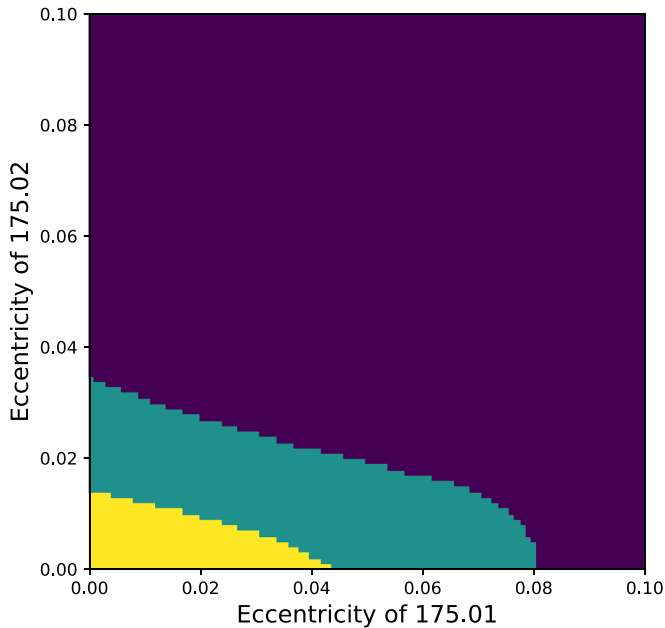
Figure 21. Parameter space in eccentricity (purple) where TTVs are likely to be detected for the L 98-59 system, assuming transit times can be measured to a precision of 2 minutes and using the forecaster planet masses. If transit times can instead be measured to 1 minute precision, TTVs are likely to be detected if the planet eccentricities are in the green region.

data at present: the best opportunity for future TTV detection with *TESS* will be in upcoming data releases, when the system is observed for five consecutive sectors.

3.3. Potential for Atmospheric Characterization

Owing to the small, bright host star, the three planets of the L 98-59 system are promising targets for follow-up atmosphere

characterization. The planets' small radii suggest that it is unlikely that they retain hydrogen-rich atmospheres (Rogers 2015; Fulton et al. 2017), but secondary atmospheres could form from volcanic outgassing and/or delivery of volatiles from comets.

To investigate the feasibility of atmosphere studies for the L 98-59 planets, we compared the expected signal-to-noise ratio of atmospheric features to that of GJ 1132b, another small planet around a nearby M-dwarf (Berta-Thompson et al. 2015). Morley et al. (2017) found that a CO_2-dominated atmosphere could be detected for GJ 1132 with a modest number of *JWST* transits or eclipses (11 transits with NIRSpec/G235M or two eclipses with MIRI/LRS). To scale these estimates for L 98-59, we used the transmission and emission spectroscopy metrics from Kempton et al. (2018), who calculated the expected signal-to-noise ratio for atmospheric features based on planet and star properties. We scaled the signal relative to each planet's transit/eclipse duration, estimated the brightness of the star based on its *K*-band magnitude, and assumed zero noise floor. We found that L 98-59 b, L 98-59 c, and L 98-59 d have transmission spectroscopy metric (TSM) values 0.8, 1.4, and 1.0 times that of GJ 1132b and emission spectroscopy metric (ESM) values 0.3, 0.4, and 0.7, respectively (Kempton et al. 2018). This implies that features in the transmission spectrum could be detected with 16, 6, or 11 transits, or 24, 13, or 4 eclipses for L 98-59 b, L 98-59 c, and L 98-59 d. Provided that *JWST* observations reach the photon limit for stars as bright as L 98-59, this system is an exciting opportunity for studying comparative planetology of terrestrial exoplanet atmospheres.

3.4. Planets in the Venus Zone

It is worth noting the possibility that the planets in the system are analogs to Venus in terms of their atmospheric evolution. Venus shares several characteristics with Earth including its
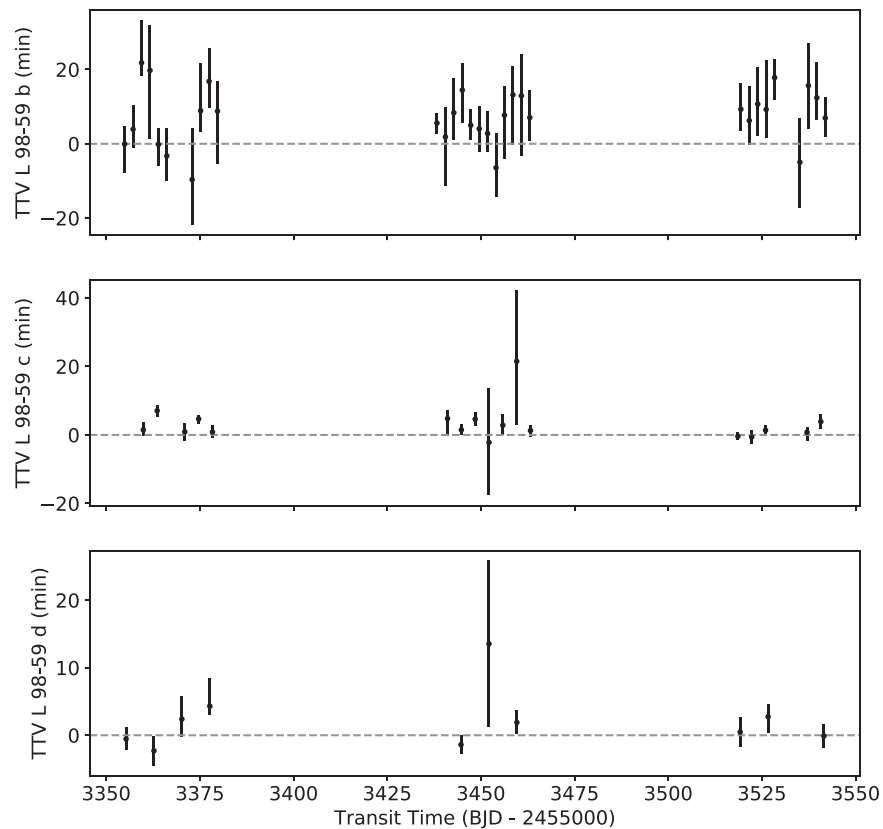
Figure 22. Observed TTVs of L 98-59. The vertical bars represent $\pm 1\sigma$ uncertainties for the observed transits, and a horizontal line shows the zero-point. The observed transit times do not meaningfully deviate from a circular orbit model.

relative composition, size, and mass. Although Venus may have previously had temperate surface conditions (Way et al. 2016), Venus eventually diverged significantly from the habitable pathway of Earth and transitioned into a runaway greenhouse state. The planet now has a high-pressure, high-temperature, and carbon-dioxide-dominated atmosphere. In our study of exoplanets and the search for life, it is vitally important that we understand why Earth is habitable and Venus is not (Kane et al. 2014). There is a need to discover planets that may have evolved into a postrunaway greenhouse state so that we can target their atmospheres for characterization with future facilities, such as *JWST* (Ehrenreich et al. 2012). However, most of the potential Venus analog candidates hitherto discovered orbit relatively faint stars (Barclay et al. 2013; Kane et al. 2013, 2018; Angelo et al. 2017).

The L 98-59 planets receive significantly more energy than the Earth receives from the Sun (a factor of between 4 and 22 more than Earth's insolation) and fall into the region that Kane et al. (2014) dubbed the Venus Zone. This is a region where the atmosphere of a planet like Earth would likely have been forced into a runaway greenhouse, producing conditions similar to those found on Venus. The range of incident fluxes within the Venus Zone corresponds to insolations of between 1 and 25 times that received by the Earth. Planets in the Venus Zone that can be spectroscopically characterized will become increasingly important in the realm of comparative planetology that aims to characterize the conditions for planetary habitability. In that respect, and considering the potential for atmospheric characterization discussed in Section 3.3, L 98-59 could become a benchmark system.

4. Conclusions

We presented the discovery of a system of three transiting, terrestrial-size planets orbiting L 98-59 (*TESS* Object of Interest TOI-175). The host star is a bright M3 dwarf ($K = 7.1$) at a distance of 10.6 pc, with $M_* = 0.313 \pm 0.014 \, M_\odot$, $R_* = 0.312 \pm 0.014 \, R_\odot$, and $T_{\rm eff} = 3367 \pm 150$ K. TFOP-led follow-up observations found no evidence of binarity or significant stellar activity. To thoroughly vet the transit signals detected in the *TESS* data, we used the software package DAVE. Our analysis ruled out significant secondary eclipses, odd–even differences, or photocenter shifts during transits, verifying their planetary nature. Using lightkurve, we also discovered that the nearby field star 2MASS 08181825-6818430, inside the *TESS* aperture of L 98-59, is an eclipsing binary system with an orbital period of $\sim$10.43 days, manifesting both primary and secondary eclipses. Utilizing *Gaia* data, we confirmed that the eclipsing binary is a background object (likely a red giant) not associated with L 98-59. This battery of tests highlights the importance of comprehensive analysis of all sources inside the *TESS* aperture.

The planets range in size from slightly smaller to slightly bigger than Earth, with radii of $0.8 \pm 0.05 R_\oplus$, $1.35 \pm 0.07 R_\oplus$, and $1.59 \pm 0.23 R_\oplus$ from inner to outer, respectively. The planetary system is quite compact, with orbital periods of 2.25 days, 3.69 days, and 7.45 days, respectively. We estimated their masses using the forecast package for probabilistic mass forecasting, confirmed the dynamical stability of the system for circular orbits, and showed that there are no significant TTVs.

TESS will continue observing the system in upcoming Sectors (9, 10, 11, 12), and it is also likely that the system will

be observed during a *TESS* Extended Mission. These observations will allow for refinement of the known planet parameters, searches for additional planets, further investigations of the dynamics of the system, as well as long-term monitoring of the host star activity.

Facilities: AAVSO, LCO, *TESS*.

Software: AstroImageJ (Collins et al. 2017), astropy (Astropy Collaboration et al. 2013, 2018), celerite (Foreman-Mackey et al. 2017; Foreman-Mackey 2018), emcee (Foreman-Mackey et al. 2013), exoplanet (Foreman-Mackey 2018), DAVE (Kostov et al. 2019), forecaster (Chen & Kipping 2017), IPython (Perez & Granger 2007), Jupyter (Kluyver et al. 2016), Lightkurve (Lightkurve Collaboration et al. 2018), Matplotlib (Hunter 2007), NumPy (van der Walt et al. 2011), Pandas (McKinney 2010), PyMC3 (Salvatier et al. 2016), SciPy (Oliphant 2007), STARRY (Luger et al. 2019), Tapir (Jensen 2013), Theano (Theano Development Team 2016), TTVFast (Deck et al. 2014), TTV2Fast2Furious (Hadden et al. 2018).

ORCID iDs

Veselin B. Kostov https://orcid.org/0000-0001-9786-1031
Joshua E. Schlieder https://orcid.org/0000-0001-5347-7062
Thomas Barclay https://orcid.org/0000-0001-7139-2724
Karen A. Collins https://orcid.org/0000-0001-6588-9574
Samuel Hadden https://orcid.org/0000-0002-1032-0783
Stephen R. Kane https://orcid.org/0000-0002-7084-0529
Laura Kreidberg https://orcid.org/0000-0003-0514-1147
Ethan Kruse https://orcid.org/0000-0002-0493-1342
Benjamin T. Montet https://orcid.org/0000-0001-7516-8308
Francisco J. Pozuelos https://orcid.org/0000-0003-1572-7707
Keivan G. Stassun https://orcid.org/0000-0002-3481-9052
Roland Vanderspek https://orcid.org/0000-0001-6763-6562
David Latham https://orcid.org/0000-0001-9911-7388
Joshua Winn https://orcid.org/0000-0002-4265-047X
Jon M. Jenkins https://orcid.org/0000-0002-4715-9460
Giada Arney https://orcid.org/0000-0001-6285-267X
Patricia Boyd https://orcid.org/0000-0003-0442-4284
Geert Barentsen https://orcid.org/0000-0002-3306-3484
Daniel Bayliss https://orcid.org/0000-0001-6023-1335
Christopher Burke https://orcid.org/0000-0002-7754-9486
David Charbonneau https://orcid.org/0000-0002-9003-484X
Jeffrey Coughlin https://orcid.org/0000-0003-1634-9672
Shawn Domagal-Goldman https://orcid.org/0000-0003-0354-9325
Courtney Dressing https://orcid.org/0000-0001-8189-0233
Mark E. Everett https://orcid.org/0000-0002-0885-7215
Thomas Fauchez https://orcid.org/0000-0002-5967-9631
Daniel Foreman-Mackey https://orcid.org/0000-0002-9328-5652
Michaël Gillon https://orcid.org/0000-0003-1462-7739
Aaron Hamann https://orcid.org/0000-0003-3996-263X
Christina Hedges https://orcid.org/0000-0002-3385-8391
Elliott P. Horch https://orcid.org/0000-0003-2159-1463
Keith Horne https://orcid.org/0000-0003-1728-0304
Steve Howell https://orcid.org/0000-0002-2532-2853
Michael Ireland https://orcid.org/0000-0002-6194-043X
Eric L. N. Jensen https://orcid.org/0000-0002-4625-7333
Ravi Kopparapu https://orcid.org/0000-0002-5893-2471
Nikole Lewis https://orcid.org/0000-0002-8507-1304
Andrew W. Mann https://orcid.org/0000-0003-3654-1602
Avi Mandell https://orcid.org/0000-0002-8119-3355
Rachel A. Matson https://orcid.org/0000-0001-7233-7508
Teresa Monsue https://orcid.org/0000-0003-3896-3059
Sarah E. Moran https://orcid.org/0000-0002-6721-3284
Caroline V. Morley https://orcid.org/0000-0002-4404-0456
Brett Morris https://orcid.org/0000-0003-2528-3409
Philip Muirhead https://orcid.org/0000-0002-0638-8822
Koji Mukai https://orcid.org/0000-0002-8286-8094
Susan Mullally https://orcid.org/0000-0001-7106-4683
Norio Narita https://orcid.org/0000-0001-8511-2981
Joseph E. Rodriguez https://orcid.org/0000-0001-8812-0565
Jason F. Rowe https://orcid.org/0000-0002-5904-1865
Avi Shporer https://orcid.org/0000-0002-1836-3120

Joseph D. Twicken ⬤ https://orcid.org/0000-0002-6778-7552
Laura Vega ⬤ https://orcid.org/0000-0002-5928-2685

References

Agol, E., Steffen, J., Sari, R., & Clarkson, W. 2005, MNRAS, 359, 567
Angelo, I., Rowe, J. F., Howell, S. B., et al. 2017, AJ, 153, 162
Anglada-Escudé, G., Amado, P. J., Barnes, J., et al. 2016, Natur, 536, 437
Astropy Collaboration, Price-Whelan, A. M., Sipőcz, B. M., et al. 2018, AJ, 156, 123
Astropy Collaboration, Robitaille, T. P., Tollerud, E. J., et al. 2013, A&A, 558, A33
Baraffe, I., Chabrier, G., Barman, T. S., Allard, F., & Hauschildt, P. H. 2003, A&A, 402, 701
Barclay, T., Burke, C. J., Howell, S. B., et al. 2013, ApJ, 768, 101
Barclay, T., Pepper, J., & Quintana, E. V. 2018, ApJS, 239, 2
Barclay, T., Quintana, E. V., Adams, F. C., et al. 2015, ApJ, 809, 7
Benedict, G. F., Henry, T. J., Franz, O. G., et al. 2016, AJ, 152, 141
Berta-Thompson, Z. K., Irwin, J., Charbonneau, D., et al. 2015, Natur, 527, 204
Boyajian, T. S., von Braun, K., van Belle, G., et al. 2012, ApJ, 757, 112
Brown, T. M., Baliber, N., Bianco, F. B., et al. 2013, PASP, 125, 1031
Bryson, S. T., Jenkins, J. M., Gilliland, R. L., et al. 2013, PASP, 125, 889
Burdanov, A., Delrez, L., Gillon, M., & Jehin, E. 2018, in Handbook of Exoplanets, ed. H. Deeg & J. A. Belmonte (Cham: Springer), 130
Charalambous, C., Martí, J. G., Beaugé, C., & Ramos, X. S. 2018, MNRAS, 477, 1414
Chen, J., & Kipping, D. 2017, ApJ, 834, 17
Ciardi, D. R., Beichman, C. A., Horch, E. P., & Howell, S. B. 2015, ApJ, 805, 16
Collins, K. A., Kielkopf, J. F., Stassun, K. G., & Hessman, F. V. 2017, AJ, 153, 77
Cutri, R. M., Wright, E. L., & Conrow, T. 2013, yCat, 2328, 0
Coughlin, J. L., Thompson, S. E., Bryson, S. T., et al. 2014, AJ, 147, 119
Deck, K. M., Agol, E., Holman, M. J., & Nesvorný, D. 2014, ApJ, 787, 132
Delrez, L., Gillon, M., Queloz, D., et al. 2018, Proc. SPIE, 10700, 107001I
Deming, D., Knutson, H., Kammer, J., et al. 2015, ApJ, 805, 132
Dittmann, J. A., Irwin, J. M., Charbonneau, D., et al. 2017, Natur, 544, 333
Dragomir, D., Teske, J., Gunther, M. N., et al. 2019, ApJL, 875, L7
Ehrenreich, D., Vidal-Madjar, A., Widemann, T., et al. 2012, A&A, 537, L2
Fabrycky, D. C., Lissauer, J. J., Ragozzine, D., et al. 2014, ApJ, 790, 146
Feinstein, A. D., Schlieder, J. E., Livingston, J. H., et al. 2019, AJ, 157, 40
Foreman-Mackey, D. 2018, Exoplanet v0.1.3, Zenodo, doi:10.5281/zenodo.2536576
Foreman-Mackey, D. 2018, RNAAS, 2, 31
Foreman-Mackey, D., Agol, E., Ambikasaran, S., & Angus, R. 2017, AJ, 154, 220
Foreman-Mackey, D., Hogg, D. W., Lang, D., & Goodman, J. 2013, PASP, 125, 306
Fulton, B. J., Petigura, E. A., Howard, A. W., et al. 2017, AJ, 154, 109
Furlan, E., & Howell, S. B. 2017, AJ, 154, 66
Gaia Collaboration, Brown, A. G. A., Vallenari, A., et al. 2018, A&A, 616, A1
Gaidos, E., Mann, A. W., Lépine, S., et al. 2014, MNRAS, 443, 2561
Gandolfi, D., Barragán, O., Livingston, J. H., et al. 2018, A&A, 619, L10
Gillon, M., Anderson, D. R., Collier-Cameron, A., et al. 2013, A&A, 552, A82
Gillon, M., Triaud, A. H. M. J., Demory, B.-O., et al. 2017, Natur, 542, 456
Hadden, S., Barclay, T., Payne, M. J., & Holman, M. J. 2018, arXiv:1811.01970
Hadden, S., & Lithwick, Y. 2014, ApJ, 787, 80
Hadden, S., & Lithwick, Y. 2016, ApJ, 828, 44
Hauschildt, P. H., Allard, F., & Baron, E. 1999, ApJ, 512, 377
Henden, A. A., Templeton, M., Terrell, D., et al. 2016, yCat, 2336, 0
Hoffman, M. D., & Gelman, A. 2014, JMLR, 15, 1593
Horch, E. P., van Altena, W. F., Howell, S. B., Sherry, W. H., & Ciardi, D. R. 2011, AJ, 141, 180
Huang, C. X., Burt, J., Vanderburg, A., et al. 2018a, ApJL, 868, L39
Huang, C. X., Shporer, A., Dragomir, D., et al. 2018b, arXiv:1807.11129
Hunter, J. D. 2007, CSE, 9, 90
Irwin, J. M., Berta-Thompson, Z. K., Charbonneau, D., et al. 2015, in 18th Cambridge Workshop on Cool Stars, Stellar Systems, and the Sun, ed. G. van Belle & H. Harris, 767
Jenkins, J. M., Seader, S., & Burke, C. J. 2017, Kepler Data Processing Handbook: A Statistical Bootstrap Test, Kepler Science Document, KSCI-19081-002
Jenkins, J. M., Twicken, J. D., McCauliff, S., et al. 2016, Proc. SPIE, 9913, 99133E

Jensen, E. 2013, Tapir: A Web Interface for Transit/Eclipse Observability, Astrophysics Source Code Library, ascl:1306.007
Kane, S. R., Barclay, T., & Gelino, D. M. 2013, ApJL, 770, L20
Kane, S. R., Ceja, A. Y., Way, M. J., & Quintana, E. V. 2018, ApJ, 869, 46
Kane, S. R., Kopparapu, R. K., & Domagal-Goldman, S. D. 2014, ApJL, 794, L5
Kempton, E. M.-R., Bean, J. L., Louie, D. R., et al. 2018, PASP, 130, 114401
Kipping, D. M. 2013a, MNRAS, 435, 2152
Kipping, D. M. 2013b, MNRAS, 434, L51
Kluyver, T., Ragan-Kelley, B., Pérez, F., et al. 2016, in Positioning and Power in Academic Publishing: Players, Agents and Agendas, ed. F. Loizides & B. Scmidt (Amsterdam: IOS Press), 87
Kostov, V. B., Mullally, S. E., Quintana, E. V., et al. 2019, AJ, 157, 124
Li, J., Tenenbaum, P., Twicken, J. D., et al. 2019, PASP, 131, 024506
Lightkurve Collaboration, Cardoso, J. V. d. M., Hedges, C., et al. 2018, Lightkurve: Kepler and TESS Time Series Analysis in Python, Astrophysics Code Library, ascl:1812.013
Lissauer, J. J., Marcy, G. W., Rowe, J. F., et al. 2012, ApJ, 750, 112
Lissauer, J. J., Ragozzine, D., Fabrycky, D. C., et al. 2011, ApJS, 197, 8
Lithwick, Y., Xie, J., & Wu, Y. 2012, ApJ, 761, 122
Livingston, J. H., Crossfield, I. J. M., Petigura, E. A., et al. 2018, AJ, 156, 277
Louie, D. R., Deming, D., Albert, L., et al. 2018, PASP, 130, 044401
Luger, R., Agol, E., Foreman-Mackey, D., et al. 2019, AJ, 157, 64
Luger, R., Agol, E., Kruse, E., et al. 2016, AJ, 152, 100
Mandel, K., & Agol, E. 2002, ApJL, 580, L171
Mann, A. W., Feiden, G. A., Gaidos, E., Boyajian, T., & von Braun, K. 2015, ApJ, 804, 64
Mayor, M., Bonfils, X., Forveille, T., et al. 2009, A&A, 507, 487
McKinney, W. 2010, in Proc. 9th Python in Science Conf., ed. S. van der Walt & J. Millman (SciPy), 51
Ment, K., Dittmann, J. A., Astudillo-Defru, N., et al. 2019, AJ, 157, 32
Morley, C. V., Kreidberg, L., Rustamkulov, Z., Robinson, T., & Fortney, J. J. 2017, ApJ, 850, 121
Morton, T. D., Bryson, S. T., Coughlin, J. L., et al. 2016, ApJ, 822, 86
Muirhead, P. S., Dressing, C. D., Mann, A. W., et al. 2018, AJ, 155, 180
Muirhead, P. S., Mann, A. W., Vanderburg, A., et al. 2015, ApJ, 801, 18
Mukai, K., & Barclay, T. 2017, tvguide: A Tool for Determining Whether Stars and Galaxies are Observable by TESS., v1.0.1, Zenodo, doi:10.5281/zenodo.823357
Newton, E. R., Charbonneau, D., Irwin, J., & Mann, A. W. 2015, ApJ, 800, 85
Nielsen, L. D., Bouchy, F., Turner, O., et al. 2019, A&A, 623, 100
Oliphant, T. E. 2007, CSE, 9, 10
Osborn, H. P., Ansdell, M., Ioannou, Y., et al. 2019, arXiv:1902.08544
Pecaut, M. J., & Mamajek, E. E. 2013, ApJS, 208, 9
Perez, F., & Granger, B. E. 2007, CSE, 9, 21
Quinn, S. N., Becker, J. C., Rodriguez, J. E., et al. 2019, arXiv:1901.09092
Quintana, E. V., Barclay, T., Raymond, S. N., et al. 2014, Sci, 344, 277
Rein, H., & Spiegel, D. S. 2015, MNRAS, 446, 1424
Ricker, G. R., Winn, J. N., Vanderspek, R., et al. 2015, JATIS, 1, 014003
Rodriguez, J. E., Quinn, S. N., Huang, C. X., et al. 2019, AJ, 157, 191
Rogers, L. A. 2015, ApJ, 801, 41
Rowe, J. F., Bryson, S. T., Marcy, G. W., et al. 2014, ApJ, 784, 45
Salvatier, J., Wiecki, T. V., & Fonnesbeck, C. 2016, Peer. J. Comp. Sci., 2, e55
Shporer, A., Wong, I., Huang, C. X., et al. 2019, AJ, 157, 178
Simcoe, R. A., Burgasser, A. J., Bernstein, R. A., et al. 2008, Proc. SPIE, 7014, 70140U
Skrutskie, M. F., Cutri, R. M., Stiening, R., et al. 2006, AJ, 131, 1163
Smith, J. C., Stumpe, M. C., Van Cleve, J. E., et al. 2012, PASP, 124, 1000
Stassun, K. G., Collins, K. A., & Gaudi, B. S. 2017, AJ, 153, 136
Stassun, K. G., Oelkers, R. J., Pepper, J., et al. 2018, AJ, 156, 102
Stassun, K. G., & Torres, G. 2016, AJ, 152, 180
Stassun, K. G., & Torres, G. 2018, ApJ, 862, 61
Stumpe, M. C., Smith, J. C., Catanzarite, J. H., et al. 2014, PASP, 126, 100
Theano Development Team 2016, arXiv:1605.02688
Tokovinin, A., Fischer, D. A., Bonati, M., et al. 2013, PASP, 125, 1336
Twicken, J. D., Catanzarite, J. H., Clarke, B. D., et al. 2018, PASP, 130, 064502
van der Walt, S., Colbert, S. C., & Varoquaux, G. 2011, CSE, 13, 22
Vanderspek, R., Huang, C. X., Vanderburg, A., et al. 2019, ApJL, 871, L24
Wang, S., Jones, M., Shporer, A., et al. 2019, AJ, 157, 51
Way, M. J., Del Genio, A. D., Kiang, N. Y., et al. 2016, GeoRL, 43, 8376
Welsh, W. F., Orosz, J. A., Aerts, C., et al. 2011, ApJS, 197, 4
Winters, J. G., Henry, T. J., Jao, W.-C., et al. 2019, AJ, 157, 216
Winters, J. G., Henry, T. J., Lurie, J. C., et al. 2015, AJ, 149, 5
Winters, J. G., Irwin, J., Newton, E. R., et al. 2018, AJ, 155, 125
Zacharias, N., Finch, C., & Frouard, J. 2017, AJ, 153, 166
Ziegler, C., Law, N. M., Baranec, C., et al. 2018, AJ, 155, 161